

Measurement Notes

Note 54

February 1998

**Design for Half Impulse Radiating Antennas:  
Lens Material Selection and Scale-Model Testing**

Gary D. Sower, Lanney M. Atchley, and Donald E. Ellibee  
EG&G MSI

W. Scott Bigelow and Everett G. Farr  
Farr Research, Inc.

Abstract

Lens material is selected and evaluated for a scale model Half Impulse Radiating Antenna (HIRA). Techniques for measuring the complex permittivity of the lens material are compared and evaluated. The high voltage break down of the lens material is evaluated. The design of the high voltage feed is modeled and its impedance profile measured by time-domain-reflectometry. A scale model of the complete HIRA is built and tested for impedance and field radiation characteristics. The most important result of these tests is that a full-scale high-voltage HIRA is feasible.

## Table of Contents

1	INTRODUCTION .....	5
1.1	OVERVIEW .....	5
1.2	PROCEDURES.....	5
2	SCALE-MODEL HIRA DESCRIPTION.....	6
2.1	PARABOLIC REFLECTOR.....	6
2.2	RADIATING ELEMENTS .....	7
2.3	COAXIAL FEED SECTION.....	9
2.4	LENS.....	10
2.5	TERMINATION.....	11
3	COMPLEX PERMITTIVITY MODEL .....	12
3.1	INTRODUCTION .....	12
3.2	MODEL .....	12
3.3	CONCLUSIONS.....	16
4	PERMITTIVITY AND PROPAGATION COEFFICIENT .....	17
4.1	BACKGROUND .....	17
4.2	TEST APPROACH.....	17
4.3	INSTRUMENTATION .....	17
4.4	COAXIAL TEST FIXTURE.....	17
4.5	TYPICAL TDR DATA.....	18
4.6	CONCLUSIONS.....	29
5	SCALE-MODEL IMPEDANCE.....	30
5.1	INTRODUCTION .....	30
5.2	PHYSICAL STRUCTURE.....	30
5.3	THEORETICAL IMPEDANCE.....	31
5.4	MEASURED IMPEDANCE .....	32
5.5	RADIATING ARM IMPEDANCE.....	33
5.6	CONCLUSIONS.....	34
6	ELECTRIC FIELD MEASUREMENTS .....	35
6.1	EQUIPMENT SETUP .....	35
6.2	PREDICTED FIELD DATA .....	35
6.3	COMPARISON THEORETICAL AND MEASURED ELECTRIC FIELDS .....	38
6.4	HIRA STEP RESPONSE AND IMPULSE RESPONSE.....	39
6.5	CONCLUSIONS.....	39
7	HIGH VOLTAGE TESTING.....	40
7.1	TESTING.....	40
7.2	WORST-CASE DC VOLTAGE REQUIREMENT.....	41
7.3	CONCLUSIONS.....	43
References.....		44

## List of Figures

Figure 2-1: Photograph of HIRA.....	6
Figure 2-2: Diagram of the HIRA.....	7
Figure 2-3: Radiating elements and their reflections in the ground plane.....	7
Figure 2-4: Detail of radiating element.....	8
Figure 2-5: Coaxial feed section and lens mount.....	9
Figure 2-6: Scale-model lens. ....	10
Figure 2-7: Scale-model lens and radiating element attachment point.....	10
Figure 2-8: Scale-model radiating element termination. ....	11
Figure 3-1: Complex permittivity of the lens material (Debye model). ....	13
Figure 3-2: Propagation coefficient of the lens material (Debye model). ....	14
Figure 3-3: Impulse response functions of the lens material. ....	15
Figure 4-1: Coaxial test fixture.....	17
Figure 4-2: Typical TDR data for the coaxial test fixture. ....	18
Figure 4-3: Dielectric constant determined from the reflection coefficient. ....	19
Figure 4-4: Dielectric constant determined from transit time.....	20
Figure 4-5: Derivatives of shorted input and lens material TDR measurements.....	23
Figure 4-6: Real and imaginary permittivity, derived from the first reflection. ....	24
Figure 4-7: Risetime comparison of reflection from short and from lens material. ....	25
Figure 4-8: Second reflection path.....	25
Figure 4-9: Averaged test cell TDR data. ....	27
Figure 4-10: Time-gated derivatives of TDR data of input section and test cell.....	27
Figure 4-11: Propagation coefficient from second reflection.....	28
Figure 4-12: Permittivity from second reflection. ....	29
Figure 5-1: Typical scale-model lens mount. ....	30
Figure 5-2: Theoretical impedance of three scale-model lens mounts. ....	31
Figure 5-3: Measured impedance of three scale-model lens mounts.....	32
Figure 5-4: Impedance of the scale-model HIRA, including radiating elements. ....	34
Figure 6-1: Scale-model E-field measurement instrumentation. ....	35
Figure 6-2: Schematic formation of a HIRA from a two-element IRA.....	36
Figure 6-3: Theoretical electric field on the centerline at 152 cm from the scale-model HIRA. ....	37
Figure 6-4: Comparison of the measured and theoretical electric fields. ....	38
Figure 6-5: HIRA impulse (A) and step (B) responses.....	39
Figure 7-1: High voltage test fixture.....	40
Figure 7-2: Simplified drawings of the lens structure for the full-scale HIRA. ....	41



## 1 INTRODUCTION

### 1.1 OVERVIEW

In support of the continuing effort to develop a Half Impulse Radiating Antenna (HIRA), a second scale-model HIRA was fabricated and tested. The design, testing and fabrication of the first scale-model HIRA are described in [1]. The first scale-model was a simple 30 cm diameter parabolic reflector with two radiating elements. The second scale-model differs from the first by the addition of a lens and the scaled simulation of a high-voltage coaxial feed system. The purpose of this effort is to evaluate the HIRA with the new lens and high voltage modifications.

### 1.2 PROCEDURES

To evaluate the high-voltage and lensed HIRA, we first selected a suitable dielectric material for the lens. Since the lens was designed using a dielectric constant of seven, we selected epoxy mixed with titanium dioxide (TiO<sub>2</sub>) for the lens material. TiO<sub>2</sub> has a dielectric constant of about 90, and epoxy has a dielectric constant in the 3 to 4 range. The first objectives were to find the proper mixture and to develop mixing and curing techniques. Conveniently, we found a commercially available mixture with a dielectric constant of seven. We then tested the high voltage standoff of the material.

After selecting the lens material and developing curing techniques, we fabricated a scale model of the high-voltage HIRA with lens. This model was used to determine the impedance profile and radiation characteristics of the HIRA. Portions of the model were modified to reduce impedance discontinuities.

We then drove the completed scale model HIRA with a fast step and measured the resultant field. We compared the output with the results of previous scale model measurements and with the theoretical field.

## 2 SCALE-MODEL HIRA DESCRIPTION

A photograph of the completed scale-model HIRA is shown in Figure 2-1.

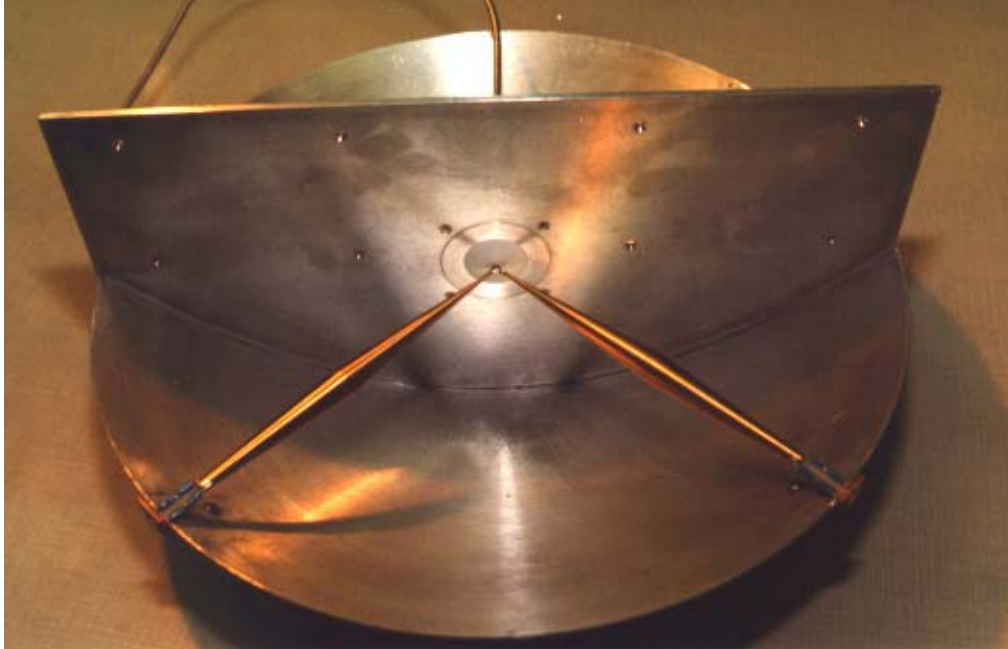


Figure 2-1: Photograph of HIRA.

### 2.1 PARABOLIC REFLECTOR

The reflector is a 30.48 cm (12 in.) diameter, spun aluminum parabola with a focal length to diameter (F/D) ratio of 0.25. This reflector size was selected for its availability and reasonable size ratio to the full-scale HIRA. The full HIRA will have same F/D ratio but will be 1.83 m (6 ft) in diameter, making the 30.48 cm reflector a 1/6-scale model.<sup>†</sup>

Since only one-half of the reflector is used, the scale-model parabolic dish is split by a ground-potential divider plate. The half of the HIRA containing the feed mount is inactive on the scale-model and will not exist on the full HIRA. The active half contains the radiating elements. Figure 2-2 shows a front view of the HIRA. In this figure, the inactive half of the parabolic reflector is omitted.

---

<sup>†</sup> Originally, the full HIRA was to have had a 3-meter reflector, for which the model reflector would have been approximately 1/10-scale. As it is, the reflector and radiating arms are now 1/6-scale, while the lens and its coaxial feed are 1/10-scale. This difference in scale is not significant to the performance of the model.

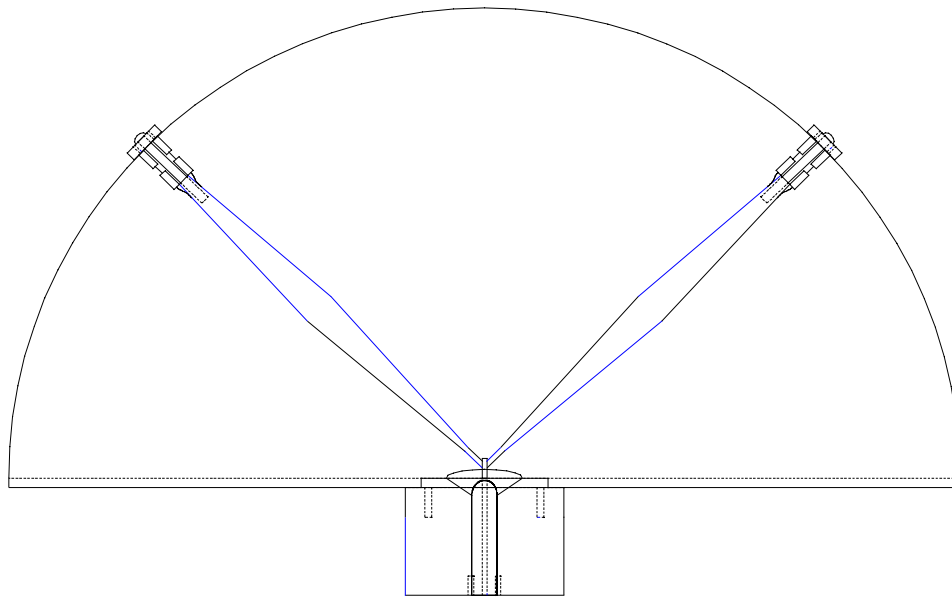


Figure 2-2: Diagram of the HIRA.

## 2.2 RADIATING ELEMENTS

The two radiating elements, visible on the radiating side of the divider plate in Figure 2-1, originate at the parabolic focal point and form a 90 degree angle with each other and a 45 degree angle to the divider plate. The elements lie in the plane formed by the focal point and the parabola's rim.

Figure 2-3A shows a simplified drawing of the radiating elements and their reflections in the ground plane (divider plate). This is the physical configuration of HIRA, where terminal 1 is driven with respect to the ground plane. Terminal 2 is the reflection of terminal 1 in the ground plane.

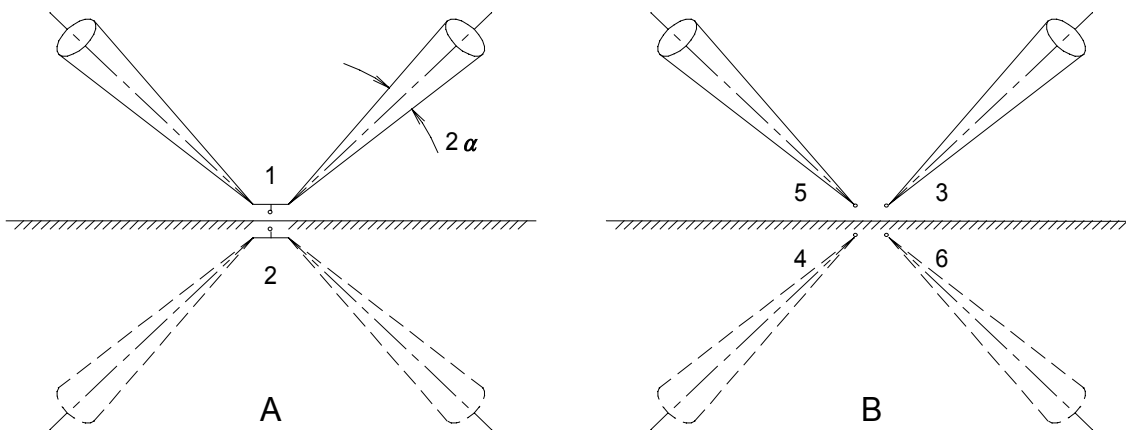


Figure 2-3: Radiating elements and their reflections in the ground plane.

Examination of Figure 2-3 reveals that driving terminal 1 with respect to terminal 2 in Figure 2-3A is identical to driving the parallel combination of terminal 3 with respect to 4 and terminal 5 with respect to 6 in Figure 2-3B. Thus the impedance of the system may be considered to be the parallel combination of two antennas. For convenience, each physical element with its associated reflection will be referred to as a conic antenna (e.g. the physical cone associated with terminal 3, and the reflection associated with terminal 4) to differentiate it from a true biconic antenna.

Each conic antenna, formed by one physical element and the reflection of the other physical element, is the equivalent of a physical cone normal to a ground plane. It has one half the impedance of a true biconic antenna formed from two physical cones. The desired impedance at the origin of the two elements is 100 ohms with respect to the ground plane. Since the impedance at the origin of the two elements is the equivalent of the parallel impedance of two conic antennas, the desired impedance of each conic antenna is 200 ohms.

The impedance of a conic antenna, normal to a conducting plane is given by:

$$Z_{cone} = \frac{377}{2\pi} \ln\left(\cot\left(\frac{\alpha}{2}\right)\right), \quad (2-1)$$

where:

$\alpha$  = cone half-angle.

Solving (2-1) for  $\alpha$ , we obtain:

$$\alpha = 2 \arctan\left(e^{\left(\frac{-Z_{cone}}{60}\right)}\right). \quad (2-2)$$

The desired impedance for the parallel combination of the HIRA radiating elements is 100 ohms. Each conic antenna is 200 ohms. Setting  $Z_{cone} = 200$  ohms, we find  $\alpha = 4.09$  degrees.

Figure 2-4 shows the design details for the scale-model radiating elements. For structural strength, the origin of the radiating elements does not terminate in a point. The 4.09 degree half-angle is maintained well past the focal point of the parabolic reflector. At some distance from the focal point, the 4.09 degree taper stops to allow the elements to narrow to the 200 ohm resistive termination at the reflector rim. The angle of narrowing is not critical and primarily keeps the element diameters from growing too large. There is also an impedance consideration, as discussed later in Section 5.5.

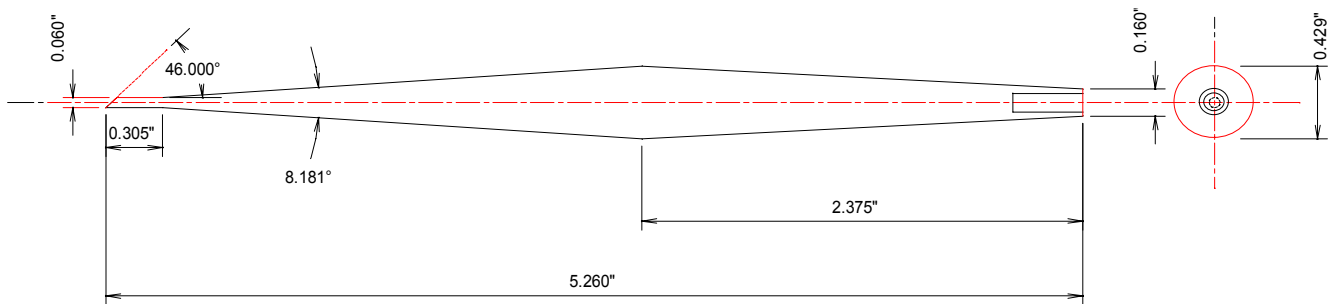


Figure 2-4: Detail of radiating element.

## 2.3 COAXIAL FEED SECTION

### 2.3.1 Description

A cut-away view of the coaxial feed section of the HIRA is shown in Figure 2-5. The aluminum housing and brass center conductor, separated by Teflon dielectric, form a 68 ohm coaxial transmission line with an SMA connector at the bottom, and a lens at the top. The curvature of the lens is exaggerated in the figure, but the ellipsoidal surface of the Teflon is accurate. The Teflon, with a dielectric constant of 2.1, is a good simulation of the insulating oil, which has a dielectric constant of about 2.2.

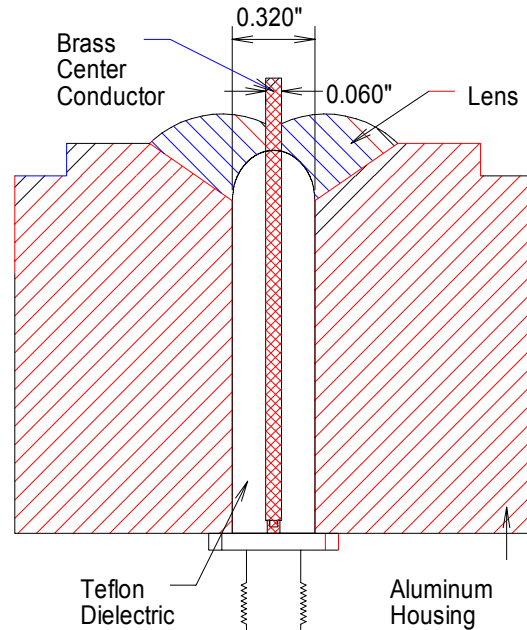


Figure 2-5: Coaxial feed section and lens mount.

### 2.3.2 Fabrication

An aluminum block forms the flared lens mount and the outer conductor of the 68 ohm coaxial feed section. The center conductor of the coaxial section is a brass rod, soldered to the center pin of an SMA connector. Teflon forms the dielectric for the feed section. The Teflon dielectric is machined, then press fit around the center conductor and into the aluminum housing. At the lens end, the Teflon is machined into an elliptical termination. The brass center conductor, the conic flare of the aluminum housing, the lens, and the elliptical Teflon end form the launch structure. The scale-model launch structure differs from the full-scale launch structure in that the scale-model center conductor is a simple cylinder, while the full-scale center conductor will be notched and tapered within the lens material. In Section 5 of this note, we discuss the impedance and shape of the center conductor within the lens material of the launch structure.

## 2.4 LENS

### 2.4.1 Description

Figure 2-6 shows a cut-away drawing of the lens. Rotating the drawing about the  $z$ -axis generates the solid lens. The divider plate lies in the  $z = 0$  plane. Figure 2-7 is a photograph of the finished lens with the radiating-elements soldered to the brass center conductor.

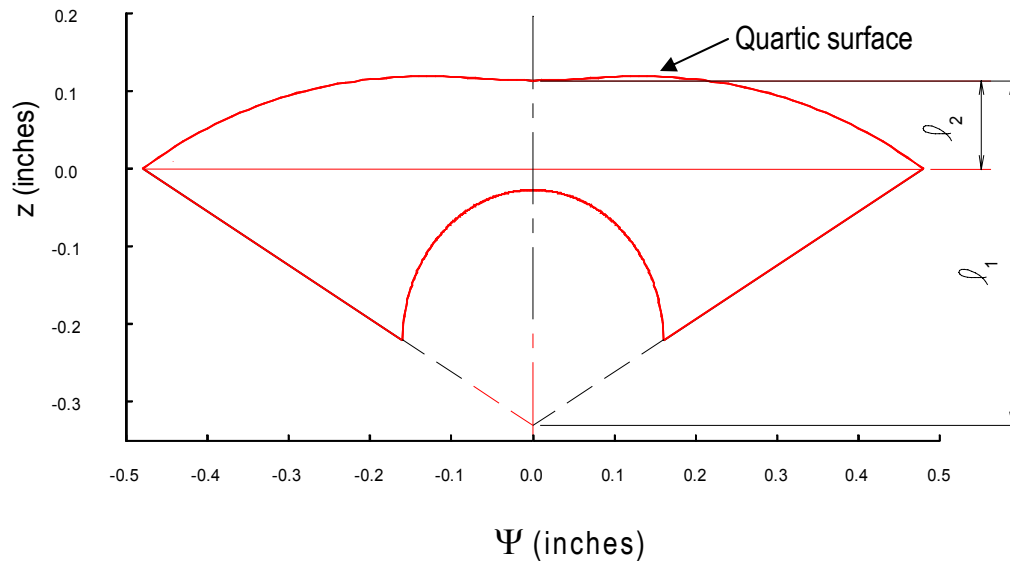


Figure 2-6: Scale-model lens.

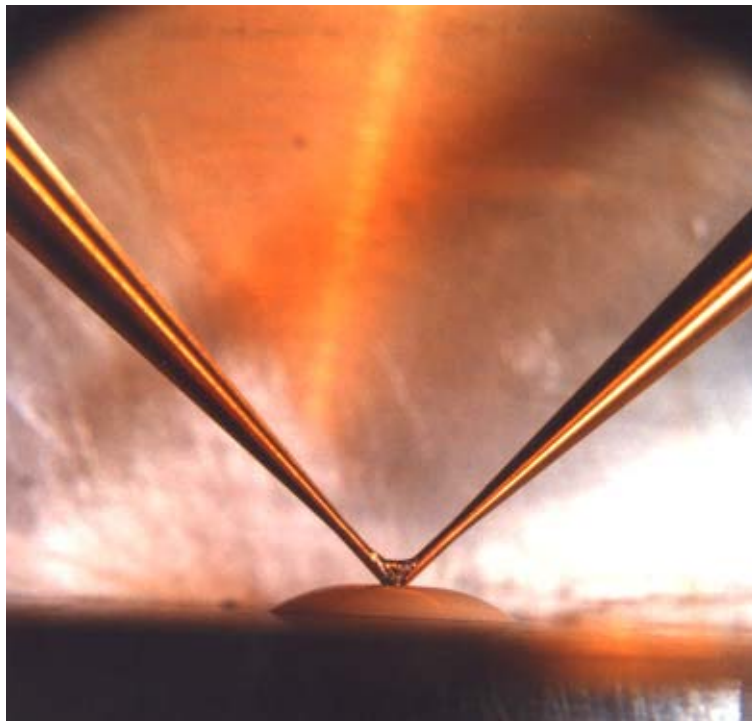


Figure 2-7: Scale-model lens and radiating element attachment point.

## 2.4.2 Fabrication

To form the lens blank we used an epoxy based paint, White-Standard #22-18000, manufactured by Ferro Corporation. The paint is a mixture of Shell EPON 828 epoxy resin, and TiO<sub>2</sub> (titanium dioxide) pigment; it is 60% TiO<sub>2</sub>, by weight. The paint is hardened with Shell TETA hardener, 13% by weight of the resin (5.2% by weight of the premixed paint).

The lens blank is fabricated by pouring the paint/hardener mixture into an oversize cylindrical mold placed on top of the lens mount assembly shown in Figure 2-5. The aluminum housing, brass center conductor, and Teflon dielectric form the lower half of the lens mold. The mixture fills the conic section and forms a lens-disk blank on the mount assembly. In order to reduce voids in the lens blank, the mixture is vacuumed as it cures, to remove trapped air and reaction product gases. The *cured* TiO<sub>2</sub>-epoxy mixture is referred to as “lens material” within this note.<sup>†</sup>

Finally, the exposed surface of the cured lens blank is machined into the shape defined by the quartic equation given in [2]:

$$\sqrt{\epsilon_r} \left( -\ell_1 + \sqrt{\Psi^2 + (\ell_1 - \ell_2 + z)^2} \right) = -\ell_2 + \sqrt{\Psi^2 + z^2}, \quad (2-3)$$

where the dimensional parameters of (2-3) are defined in Figure 2-6, and  $\epsilon_r$  is the relative permittivity of the lens material.

## 2.5 TERMINATION

The radiating elements of the full-scale HIRA will be terminated using eight Dale NS-10, wire-wound, 100 ohm resistors. Two parallel strings of four resistors in series will comprise the termination. To simulate the full-scale termination, the scale-model HIRA is terminated with four RN55 metal film 200 ohm, 1/8 watt resistors., arranged in two parallel strings of two resistors in series. Figure 2-8 is a photograph of the scale-model resistor termination.

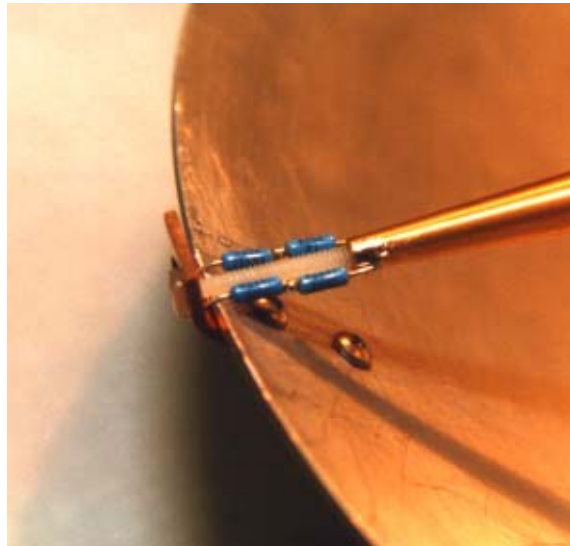


Figure 2-8: Scale-model radiating element termination.

---

<sup>†</sup> No measurements were made on uncured materials.

### 3 COMPLEX PERMITTIVITY MODEL

#### 3.1 INTRODUCTION

It is instructive to model the complex permittivity of the lens material based on the theory of relaxation processes. From [3]:

“Relaxation is a process. The term applies, strictly speaking, to linear systems where a response and a stimulus are proportional to one another in equilibrium. Relaxation is a delayed response to a changing stimulus in such a system. Dielectric relaxation occurs in dielectrics, that is in insulating materials with negligible or small electrical conductivity. The stimulus is almost always an electric field, the response a polarization. The time lag between field and polarization implies an irreversible degradation of free energy to heat.”

In [4], V. V. Daniel tells us that relaxation is a property of a passive network or system. This results in several interesting and equivalent properties of the system:

1. The passive character of the network requires that the responses decay with time, and hence all the critical (natural) frequencies of the system must have a negative real part. The poles of the natural frequencies must lie in the left half of the complex frequency plane. This condition is referred to as the *stability requirement*, which follows from the fact that the transient response of a passive system must die out. The natural behavior cannot grow without limit.
2. A system cannot have a stable response (one that will not take off on its own) unless the pertinent system function (dielectric permittivity in our case) is *analytic in the right half of the complex frequency plane*.
3. The system must also be *causal*: a response cannot occur before the stimulus is applied.

The real and the imaginary parts of the natural frequency response of a passive system form a *Hilbert transform-pair*. If either component is known over all frequencies, the other can be calculated exactly.

#### 3.2 MODEL

The complex permittivity of a dielectric may be defined in terms of the (complex) incident electric field and the static “dipolar” polarization as:

$$\varepsilon(\omega) = \varepsilon_{\infty} + 4\pi \frac{P_D(\omega, t)}{E_{inc}(\omega, t)}, \quad (3-1)$$

where  $\varepsilon$ ,  $P$ , and  $E$  are complex quantities and  $\varepsilon_{\infty} = n^2$  defines the optical dielectric constant. The polarization can usually be approximated by a single relaxation time,  $\tau$ , giving for the case of zero initial polarization:

$$\varepsilon(\omega) = \varepsilon_{\infty} + \frac{\varepsilon_s - \varepsilon_{\infty}}{1 + j\omega\tau}, \quad (3-2)$$

where  $\epsilon_s$  is the static (low frequency) dielectric constant. This is the Debye equation. It can be separated into real and imaginary parts as:

$$\epsilon = \epsilon' - j\epsilon'' , \quad (3-3)$$

where

$$\epsilon'(\omega) = \epsilon_\infty + \frac{\epsilon_s - \epsilon_\infty}{1 + \omega^2 \tau^2} , \quad (3-4)$$

and

$$\epsilon''(\omega) = \frac{(\epsilon_s - \epsilon_\infty)\omega\tau}{1 + \omega^2 \tau^2} . \quad (3-5)$$

These are shown in Figure 3-1, for values of  $\epsilon_s$ ,  $\epsilon_\infty$ , and  $\tau$  that approximate the results of the measurements.<sup>†</sup>

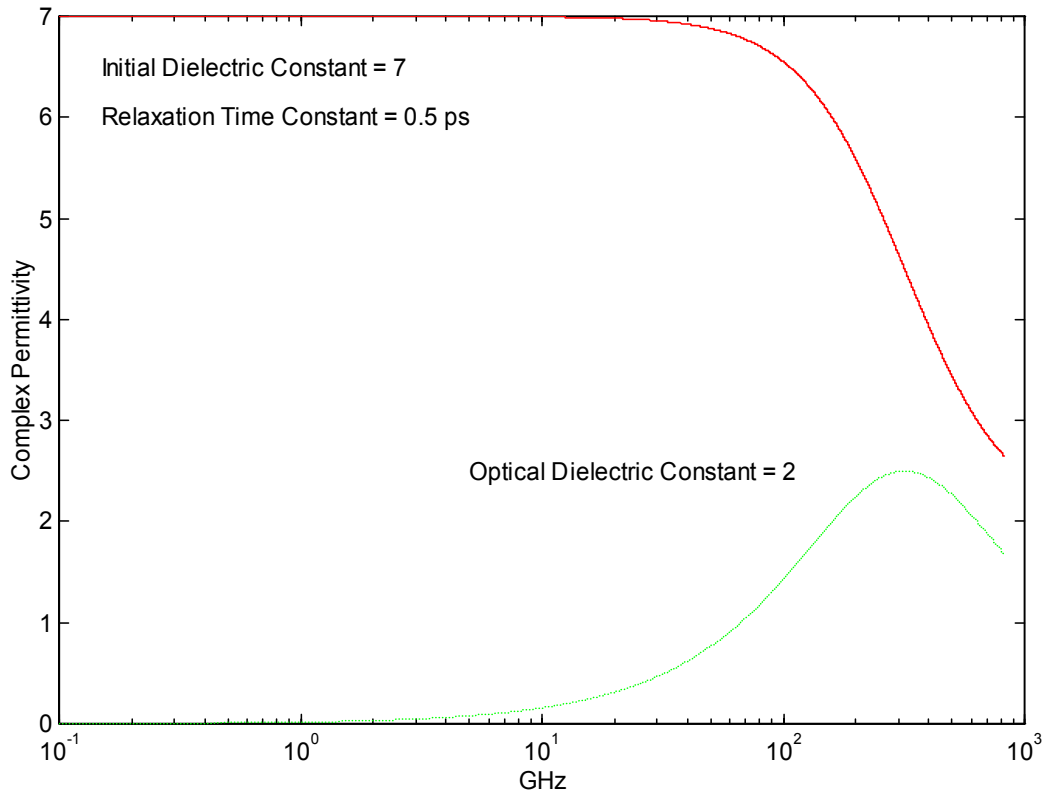


Figure 3-1: Complex permittivity of the lens material (Debye model).

<sup>†</sup> The solid line is the real part; the broken line is the imaginary part. We follow this convention is throughout the remainder of this note.

The propagation coefficient of an electromagnetic wave in the lens material is :

$$\gamma(\omega) = \alpha + j\beta = j \frac{\omega}{c} \sqrt{\varepsilon(\omega)}, \quad (3-6)$$

where  $c$  is the speed of light, and  $\alpha$  and  $\beta$  are real functions of  $\omega$ . The real and imaginary parts of the propagation coefficient (in units of inverse meters) are presented in Figure 3-2.

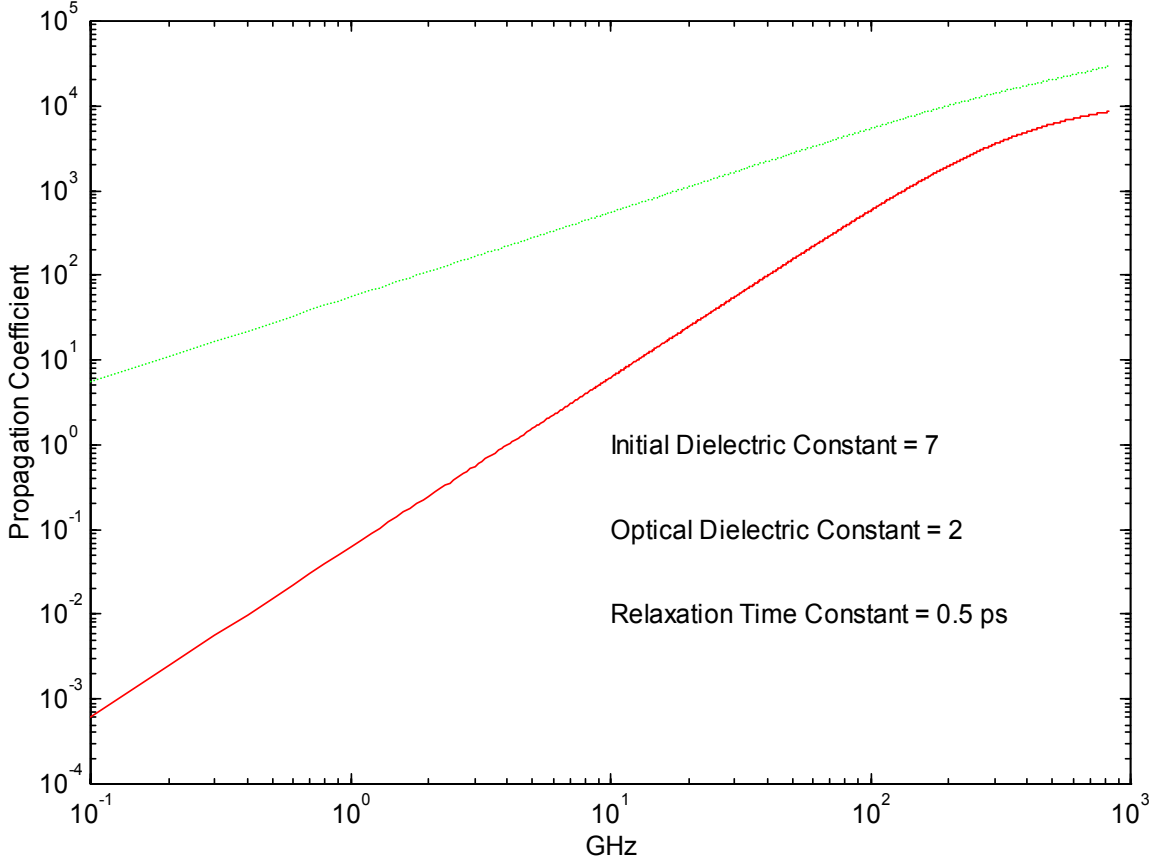


Figure 3-2: Propagation coefficient of the lens material (Debye model). Units of the coefficient are inverse meters.

The propagation of a field through a given length,  $\ell$ , of material is defined by:

$$E(\ell, \omega) = E_0(\omega) e^{-\gamma(\omega)\ell}. \quad (3-7)$$

The real part of the exponent gives the attenuation of the signal at each frequency, and the imaginary part gives the phase delay.

The time domain results for our model, obtained from (3-7) by application of the inverse Laplace transform, are shown in Figure 3-3 for several lengths of lens material. The bell-shaped curve for each length is the impulse response function for that length. It is the response to a delta-function impulse at  $t = 0$ . The step response functions would be the integrals of the impulse response functions. The time at which the response occurs is the propagation time

through that length of dielectric. The vertical dashed line in each curve is the calculated delay based upon the initial (static or low-frequency) dielectric constant (7.0), as:

$$t_D = \frac{\ell}{c} \sqrt{\epsilon_s} . \quad (3-8)$$

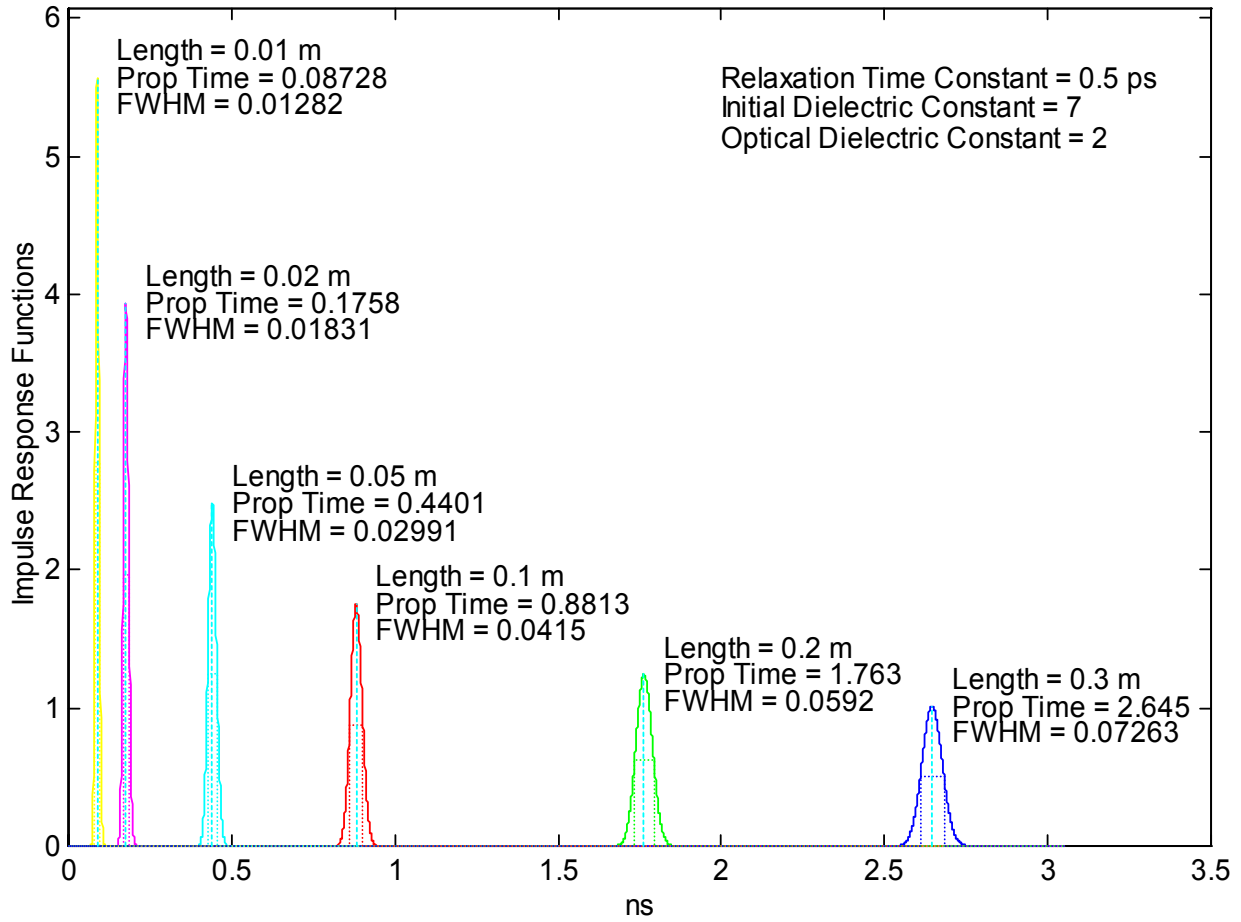


Figure 3-3: Impulse response functions of the lens material.

The peak of each curve occurs almost exactly at the theoretical delay time predicted by the static dielectric constant. The response widths (in nanoseconds) can be quantified by the full-width-at-half-maximum (FWHM), as indicated by the width of the dashed box within each curve. The following table lists the pulse delay and width data depicted in Figure 3-3. It shows

that the pulse delay varies linearly with path length, while the pulse width varies as the square root of the path length.<sup>†</sup>

Tabulation of the information presented in Figure 3-3 ( $\tau = 5$ ps, $\epsilon_s = 7$ , $\epsilon_- = 2$ )						
Length (L)	Delay (D)	D/L	(D/L)/mean	FWHM (W)	W/(L <sup>1/2</sup> )	(W/L)/mean
0.01	0.08728	8.72800	0.99316	0.01648	0.16480	0.98742
0.02	0.17520	8.76000	0.99680	0.02380	0.16829	1.00834
0.05	0.44010	8.80200	1.00158	0.03723	0.16650	0.99759
0.1	0.88070	8.80700	1.00215	0.05310	0.16792	1.00609
0.2	1.76300	8.81500	1.00306	0.07507	0.16786	1.00576
0.3	2.64500	8.81667	1.00325	0.09094	0.16603	0.99480
sum		52.72867			1.00140	
mean		8.78811			0.16690	

### 3.3 CONCLUSIONS

The implications of these complex permittivity modeling results for the HIRA lens are:

1. The maximum path length through the lens is about 10 cm. The impulse response function through this path will be about 52 ps.
2. The minimum path length through the lens is about 3 cm. The impulse response function through this path will be about 30 ps.
3. Convolution of the 30–50 ps response function with a pulser waveform having a risetime in excess of 100 ps will degrade the measured risetime by at most ten percent.

---

<sup>†</sup> The observed relationship between impulse response width and propagation length differs from that which characterizes high-frequency skin effects in coaxial cable conductors, where the width of the impulse response is proportional to the propagation length. In that case, the real part of the propagation coefficient is proportional to the square root of the frequency and the imaginary part is directly proportional to frequency ( $\gamma \propto a\sqrt{\omega} + jb\omega$ ). Here, we are concerned with the portion of the permittivity curve (Figure 3-1) below 10 GHz, where (for a relaxation time constant of 0.5 ps) the real part of the Debye permittivity, (3-4), is constant to first order, and the imaginary part, (3-5), increases linearly with frequency. In this frequency regime, Figure 3-2 shows that the real part of the propagation coefficient increases as the square of the frequency, while the imaginary part increases linearly with frequency ( $\gamma \propto a\omega^2 + jb\omega$ ). The difference in the frequency dependence of the real parts of the propagation coefficients explains the observed pulse-width-propagation-length behavior.

## 4 PERMITTIVITY AND PROPAGATION COEFFICIENT

### 4.1 BACKGROUND

Two indirectly measurable quantities are important for the lens material. First, the ray optics design requires a lens material with a dielectric constant (real part of the permittivity) very close to seven. Second, the lens material must have a low attenuation constant in order to maximize the energy propagation. In terms of the permittivity, the real portion must be close to seven, and the imaginary portion must be close to zero. Since the lens will not have perfect transmission, there will be some imaginary component to the permittivity.

### 4.2 TEST APPROACH

The permittivity of the lens material was measured by using it as the dielectric material in a coaxial test fixture. By a TDR measurement of the fixture, the real portion of the permittivity can be determined from either the reflection coefficient,  $\rho$ , or from the velocity of propagation through the fixture. Information on the imaginary portion of the permittivity is contained within the risetime of the reflected pulse.

### 4.3 INSTRUMENTATION

We used the Tektronix 11801B digital sampling oscilloscope with the SD 24, 20 GHz, dual-channel, TDR sampling head to measure the sample of lens material. The coaxial test fixture containing the sample was always connected directly to the SD 24 head, with no intervening cable.

### 4.4 COAXIAL TEST FIXTURE

A simplified drawing of the coaxial test fixture used to measure the lens material is shown in Figure 4-1. The 18.1 cm (7.125 in.) air-filled input section on the left forms a 50 ohm coaxial reference line. This 50 ohm section has a type N input, as shown on the left in the figure. The 50 ohm section may be terminated at its open end with either a machined brass shorting disk, or the test cell. The test cell is shown on the right of the figure. This cell may be left empty or filled with lens material. When filled, the exposed end of the lens material is machined flush, so that the cell remains 14.99 cm (5.902 in.) long. This cell length gives a 1.0 ns round-trip transit time in air. Thus, the round-trip time in nanoseconds is numerically the square root of the relative dielectric constant of the material filling the test cell.

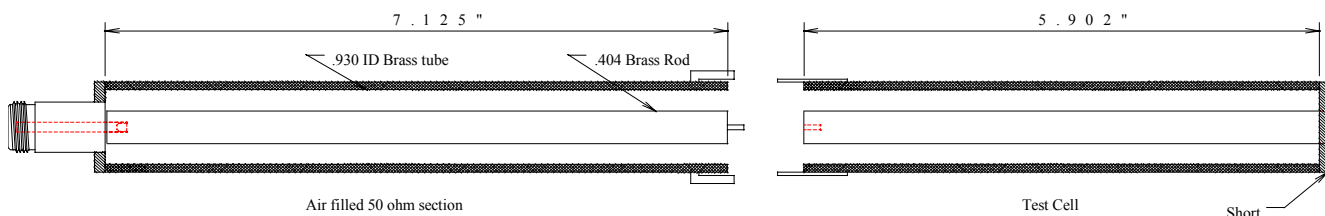


Figure 4-1: Coaxial test fixture.

## 4.5 TYPICAL TDR DATA

### 4.5.1 Permittivity Calculated from the Measured Reflection Coefficient

Figure 4-2 shows typical TDR data for the test fixture. The upper trace is for the air-filled input section terminated with the machined brass short. The lower trace is for the complete test fixture, with lens material filling the test cell.

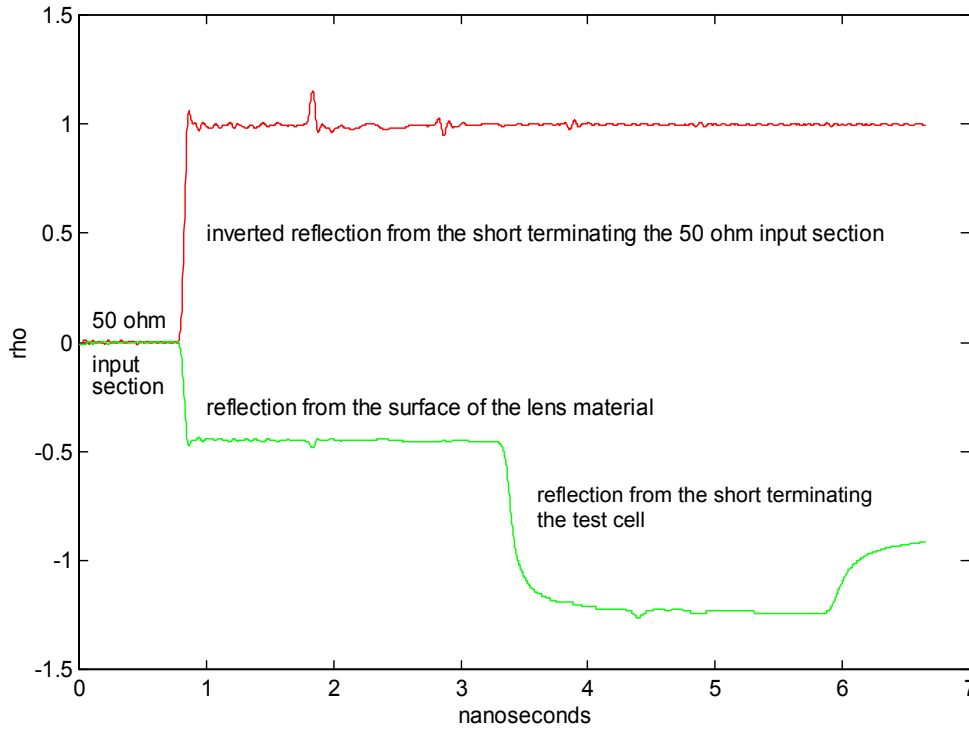


Figure 4-2: Typical TDR data for the coaxial test fixture.

The baseline, at  $\rho = 0$ , represents the 50 ohm air-filled section. The reflection from the short (top trace) has been inverted for clarity of presentation. The measured reflection coefficient is negative one. The reflection data from the test cell (filled with lens material) display two negative-going steps. The first step, from  $\rho = 0$  to  $\rho = -0.45$ , is the reflection at the interface between the air-filled section and the lens material filling the test cell. The second, rounded step is the reflection from the brass short terminating the test cell. A multiple reflection within the test cell is apparent at the end of the trace (positive-going, rounded step).

We now seek an expression for the permittivity of the lens material in terms of the measured test cell reflections. The impedance,  $Z$ , of a coaxial structure may be found in any transmission line handbook as:

$$Z = \frac{Z_0}{2\pi} \ln\left(\frac{D}{d}\right) \frac{1}{\sqrt{\epsilon_r}}, \quad (4-1)$$

where:

- $Z_0 = 377$  ohms,
- $D$  = outer conductor diameter,
- $d$  = inner conductor diameter,
- $\epsilon_r$  = relative permittivity of material filling the line (lens material).

The reflection coefficient,  $\rho$ , at a boundary between regions of differing impedance is given by:

$$\rho = \frac{Z_2 - Z_1}{Z_1 + Z_2}, \quad (4-2)$$

where:

- $Z_1$  = input side impedance (50 ohm air line in the test fixture),
- $Z_2$  = output side impedance (lens material in the test fixture).

For the air-filled test fixture,  $Z_1$  in (4-2) is 50 ohms, as calculated using (4-1) and the construction shown in Figure 4-1.  $Z_2$  is derived from the measured quantity,  $\rho$ , by solving (4-2) for  $Z_2$  and setting  $Z_1$  to 50 ohms:

$$Z_2 = 50 \frac{1 + \rho}{1 - \rho}. \quad (4-3)$$

By equating (4-1) and (4-3), and solving for  $\epsilon_r$ , we obtain the following equation, which allows the relative permittivity of the lens material to be calculated from its reflection coefficient as:

$$\epsilon_r = \left( \frac{60 \left( \frac{1 - \rho}{1 + \rho} \right) \ln \left( \frac{D}{d} \right)}{50} \right)^2. \quad (4-4)$$

By applying (4-4) to the reflection coefficient data for the test cell filled with lens material, we obtain the dielectric constant for the lens material, as shown in Figure 4-3. This figure shows that the measured reflection coefficient of -0.45 (see Figure 4-2) corresponds to a lens material relative permittivity of about 7.0.

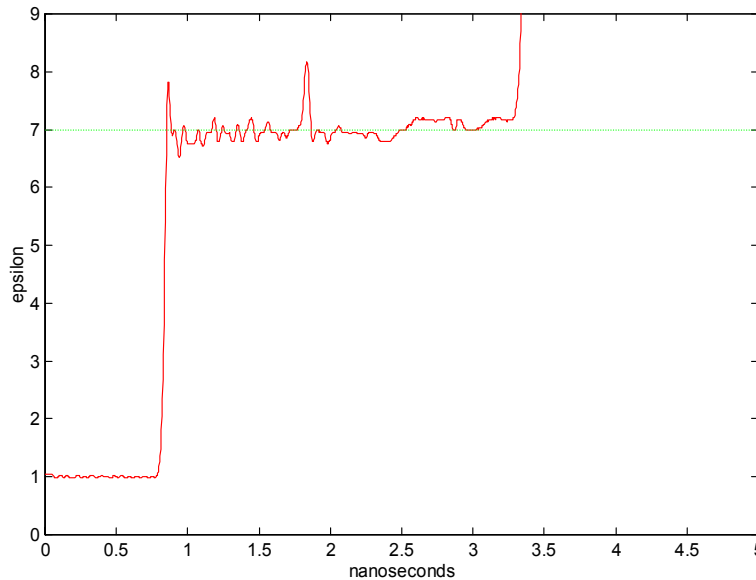


Figure 4-3: Dielectric constant determined from the reflection coefficient.

#### 4.5.2 Permittivity Calculated from the Transit Time

The permittivity is also related to the round-trip transit time of the TDR pulse through the test cell. It is calculated from:

$$\epsilon_r = \left( \frac{c}{v_p} \right)^2 = \left( \frac{ct}{2\ell} \right)^2, \quad (4-5)$$

where:

- $\epsilon_r$  = relative permittivity of the lens material,
- $v_p$  = velocity of propagation through the lens material,
- $\ell$  = length of the test cell (14.99 cm),
- $c$  = speed of light in vacuum (29.98 cm/ns),
- $t$  = round-trip transit time through the test cell (nanoseconds).

Figure 4-4 shows the derivative of the test cell TDR measurement. The time between the negative peaks of the derivative gives a round-trip transit time of about 2.56 ns, which corresponds to a permittivity of 6.5. Note the noise introduced by numerical differentiation of the data. The noise is most apparent at late times where the original measurement is at its lowest value. In later data, this problem is mitigated by averaging repeated measurements.

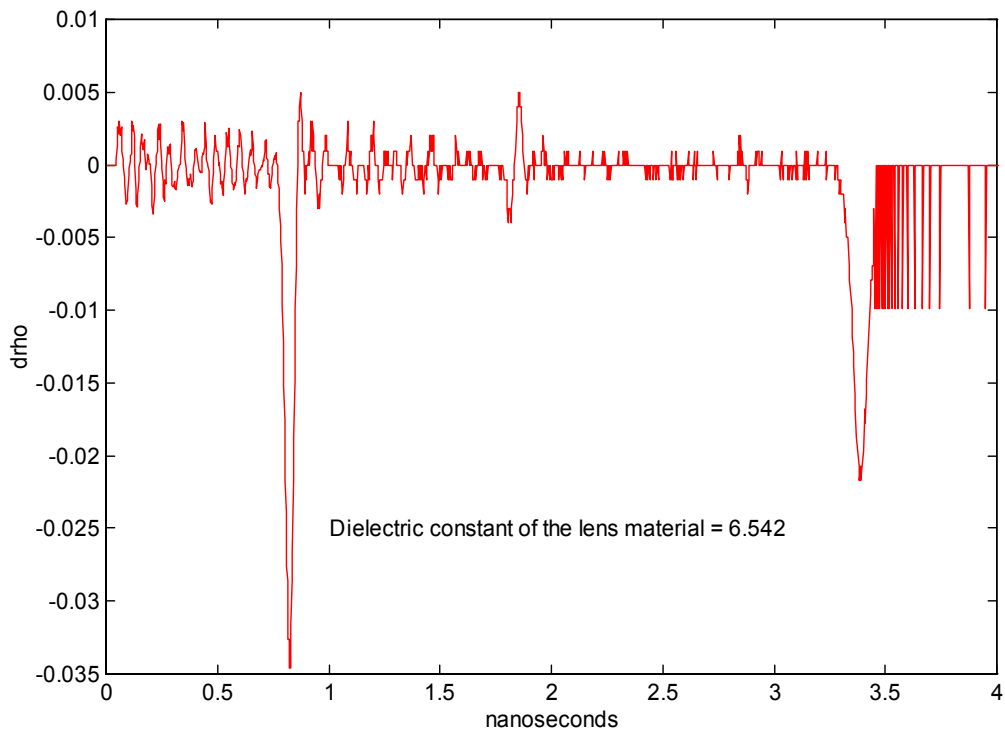


Figure 4-4: Dielectric constant determined from transit time.

The accuracy of the dielectric constant, as calculated from the transit time through the test cell, depends on our ability to select comparable measurement positions on the negative peaks of the TDR derivative. Although the error in the dielectric constant is proportional to the

square of the measurement error, the difference between the previously measured value ( $\epsilon_r = 7$ ) and the current value ( $\epsilon_r = 6.5$ ) is too great to attribute solely to a combination of measurement and analysis errors. The probable explanation for the apparent discrepancy is that the value,  $\epsilon_r = 7$ , results from a low frequency measurement (dc value of  $\rho$ ), while the value,  $\epsilon_r = 6.5$ , results from a high frequency measurement (the transit time of the leading edge of the TDR pulse). Measurement of the complex permittivity in the frequency domain, as discussed below, supports this conclusion.

### 4.5.3 Complex Permittivity Measured from the First Reflection

#### 4.5.3.1 Equation Derivation

The relative complex permittivity of the lens material,  $\epsilon_r$ , defined by (3-3) in terms of real and imaginary parts as  $\epsilon' - j\epsilon''$ , can be obtained from three reflectivity measurements, all made at the input of the coaxial test cell. Although we shall see that just two measurements are sufficient with our test cell geometry, Figure 4-1, we begin with the more general approach.

The first measurement is of a short at the input of the test cell. This gives the response of the TDR system and drive cable. We will need to deconvolve this response from the other measured test cell responses. We used a step TDR to obtain the waveform,  $\rho_0(t)$ , and we calculated the derivative,  $\rho'_0(t)$ , to obtain the impulse response.

The second measurement is of the empty (air-filled) input of the test cell. This measurement produces a reflection coefficient,  $\rho_1(t)$ , which is a step function with finite risetime. We calculate the derivative of this waveform to obtain  $\rho'_1(t)$ , which is the convolution of the system impulse response with the impulse response of the air-filled test cell,  $\rho_A(t)$ :

$$\rho'_1(t) = \rho_A(t) \otimes \rho'_0(t). \quad (4-6)$$

The frequency domain response of the air cell to a delta function excitation is  $\rho_A(\omega)$ , the fast Fourier transform (*fft*) of  $\rho_A(t)$ :

$$\rho_A(\omega) = \text{fft}(\rho_A(t)) = \frac{\text{fft}(\rho'_1(t))}{\text{fft}(\rho'_0(t))} \quad (4-7)$$

The third measurement is obtained with the test cell filled with lens material. The input section is now terminated by lens material. This leads to  $\rho'_2(t)$  and  $\rho_L(t)$ , and to expressions analogous to (4-6) and (4-7), where  $\rho'_2(t)$  is the convolution of the system impulse response with the (first reflection) impulse response,  $\rho_L(t)$ , of the lens-material-terminated input section.

The reflection coefficient at the input of the test cell is related to the impedance discontinuity there by

$$Z = Z_i \frac{1 + \rho(\omega)}{1 - \rho(\omega)}, \quad (4-8)$$

where  $Z_i$  is the complex, frequency-dependent impedance of the air-filled input section. Since the impedance of the test cell section is inversely proportional to the square root of the permittivity of the fill material, and since the relative permittivity of air is unity, we obtain the following expression for the complex relative permittivity of the lens material:

$$\varepsilon_r(\omega) = \varepsilon' - j\varepsilon'' = (Z_A/Z_L)^2, \quad (4-9)$$

where, from (4-8),

$$Z_A/Z_L = \left( \frac{1 + \rho_A(\omega)}{1 - \rho_A(\omega)} \right) \left( \frac{1 - \rho_L(\omega)}{1 + \rho_L(\omega)} \right). \quad (4-10)$$

Thus, from (4-7) for  $\rho_A(\omega)$ , and the analogous expression for  $\rho_L(\omega)$ , we finally obtain:

$$\varepsilon' + j\varepsilon'' = \left( \frac{\text{fft}(\rho'_0(t)) + \text{fft}(\rho'_1(t))}{\text{fft}(\rho'_0(t)) - \text{fft}(\rho'_1(t))} \right)^2 \left( \frac{\text{fft}(\rho'_0(t)) + \text{fft}(\rho'_2(t))}{\text{fft}(\rho'_0(t)) - \text{fft}(\rho'_2(t))} \right)^2, \quad (4-11)$$

where:

- $\varepsilon'$  = real part of the relative permittivity,
- $\varepsilon''$  = imaginary part of the relative permittivity,
- $\rho'_0$  = derivative of the reflection coefficient of the shorted, air-filled input section,
- $\rho'_1$  = derivative of the reflection coefficient of the shorted, air-filled test cell,
- $\rho'_2$  = derivative of the reflection coefficient of the shorted, lens-material-filled test cell.

For the test fixture used to measure the lens material (Figure 4-1), the air-filled 50 ohm input section is identical to the air-filled input of the test cell. The reflection coefficient,  $\rho_1$ , is a constant; so its derivative is zero. Thus, (4-11) reduces to:

$$\varepsilon' + j\varepsilon'' = \left( \frac{\text{fft}(\rho'_0(t)) + \text{fft}(\rho'_2(t))}{\text{fft}(\rho'_0(t)) - \text{fft}(\rho'_2(t))} \right)^2. \quad (4-12)$$

This result suggests that a measurement of the reflection of the input step at a perfect short, combined with a measurement of the reflection of that same step from the lens material, are sufficient to determine the permittivity of the lens material.

#### 4.5.3.2 Data

Figure 4-2 shows the recorded reflection coefficients corresponding to (4-12). The shorted, 50 ohm air-filled input section, corresponding to  $\rho_0$ , is the positive (inverted) trace. The test cell filled with lens material, corresponding to  $\rho_2$ , is the negative, stepped trace.

Differentiating and windowing  $\rho_0$  and  $\rho_2$  results in Figure 4-5. The differentiation forces both traces to return to zero to allow Fourier transformation. The time-gating window (not shown at its true magnitude of unity) removes both the first reflection (the step from  $\rho = 0$  to  $\rho = -0.45$ ) and spurious baseline noise, by setting all data outside the window to zero.

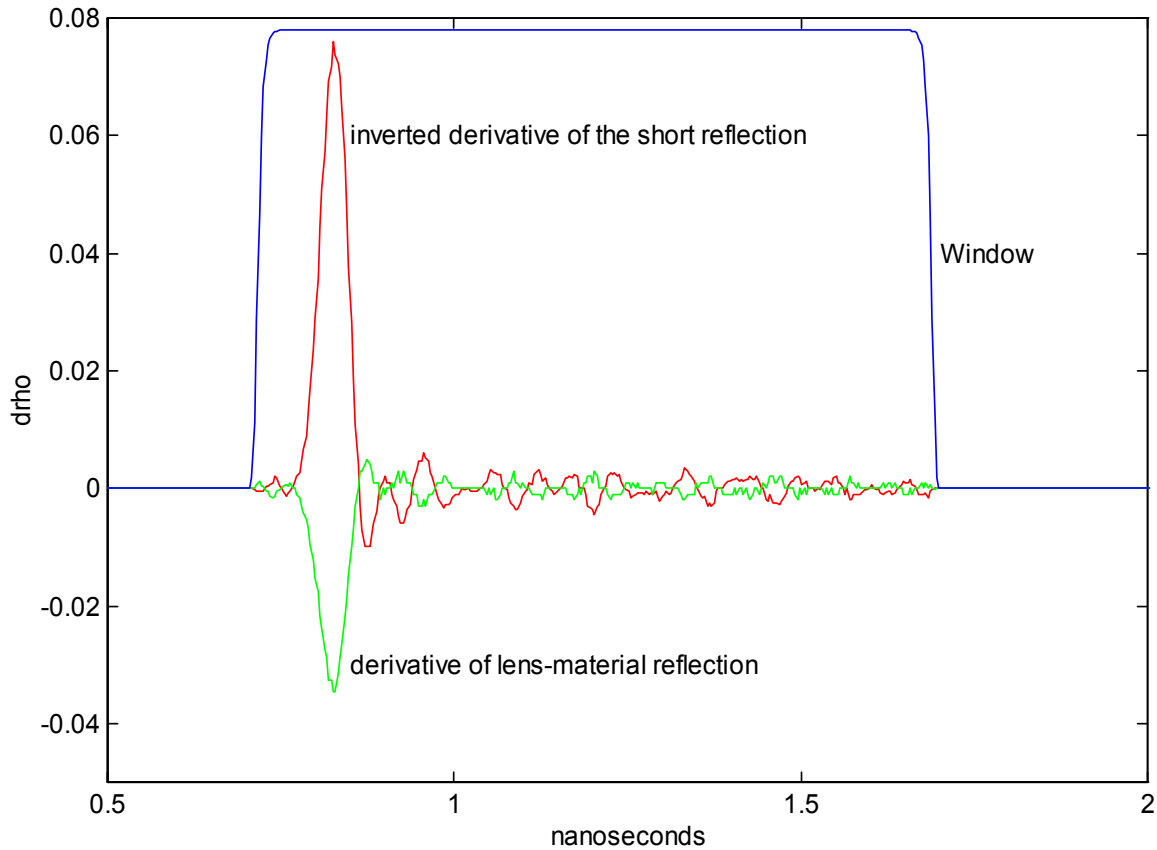


Figure 4-5: Derivatives of shorted input and lens material TDR measurements. The time-gating window was used to suppress irrelevant data.

By Fourier transforming the two derivatives shown in Figure 4-5, and applying (4-12), one generates the complex permittivity. The real and imaginary parts of the complex permittivity are shown in Figure 4-6. In the figure, the real portion of the permittivity is the top trace, near the value of 7.1, falling slightly as frequency increases. Note that the low-frequency permittivity shows good agreement with the value obtained from the reflection coefficient, and the high-frequency permittivity falls off to about the value obtained by the transit-time measurement. The imaginary part of the permittivity starts near zero, rising as frequency increases. However, it rises much more rapidly than the Debye model (see Section 3, Complex Permittivity Model) predicts. We believe this to be a result of a measurement problem, as discussed below.

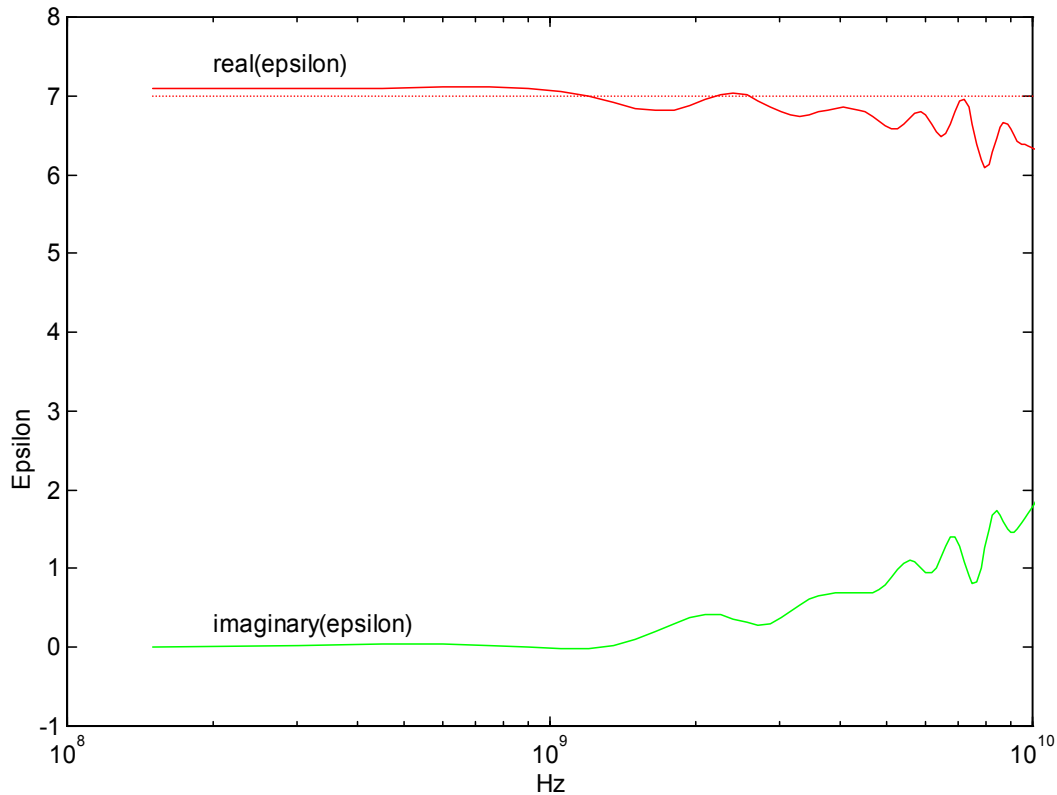


Figure 4-6: Real and imaginary permittivity, derived from the first reflection.

There is a problem with this permittivity measurement. The information is derived from only the initial reflection from the air-lens-material boundary. Since this reflected wave has not traveled through the lens material, the information it contains arises only from the degradation of the risetime. Unfortunately, the degradation is so small that the 11801B cannot accurately distinguish the difference between the risetime of the reflection from the shorted input section and the risetime of the reflection from the lens-material.

To demonstrate the problem with the measured risetimes, Figure 4-7 shows the derivative measurements of Figure 4-5, normalized, overlaid, and expanded. Comparison of the full-width-at-half-maximum (FWHM) of the two reflection derivatives in Figure 4-7 reveals that the risetimes are identical to within the measurement capability. Thus, the risetime degradation due to passage through the lens material is below the measurement threshold, and the calculated imaginary component of the permittivity is meaningless. The attenuation constant,  $\alpha$ , cannot be determined.

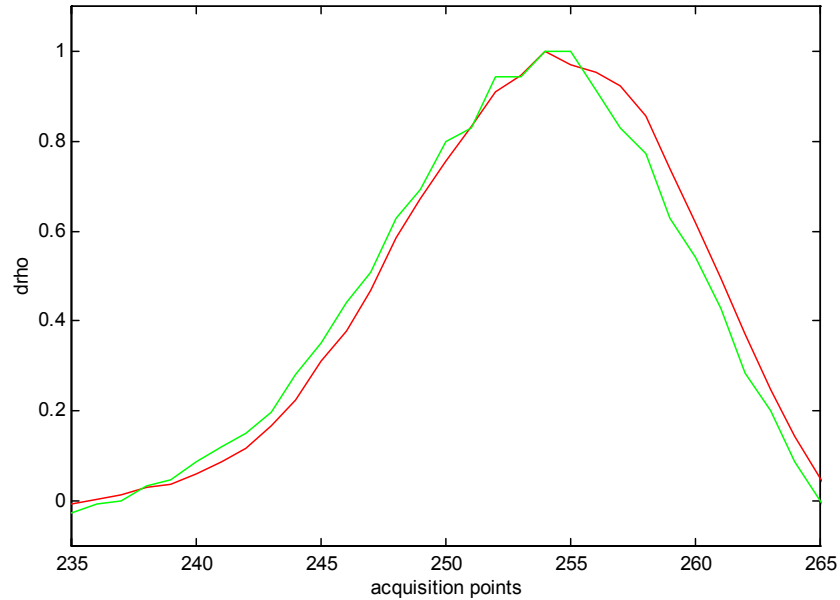


Figure 4-7: Risetime comparison of reflection from short and from lens material.

#### 4.5.4 Complex Permittivity Measured from the Second Reflection

##### 4.5.4.1 Equation Derivation

The second reflection (occurring between three and four nanoseconds in the lens material in Figure 4-2) has a significantly slower risetime, as a result of its passage through the lens material. The slow risetime suggests that we can recover the complex portion of the permittivity by using the second reflection. The second reflection occurs when the TDR pulse crosses the air-to-lens-material boundary, reflects from the short terminating the test cell, and re-crosses the lens-material-to-air boundary. Figure 4-8 illustrates the path.

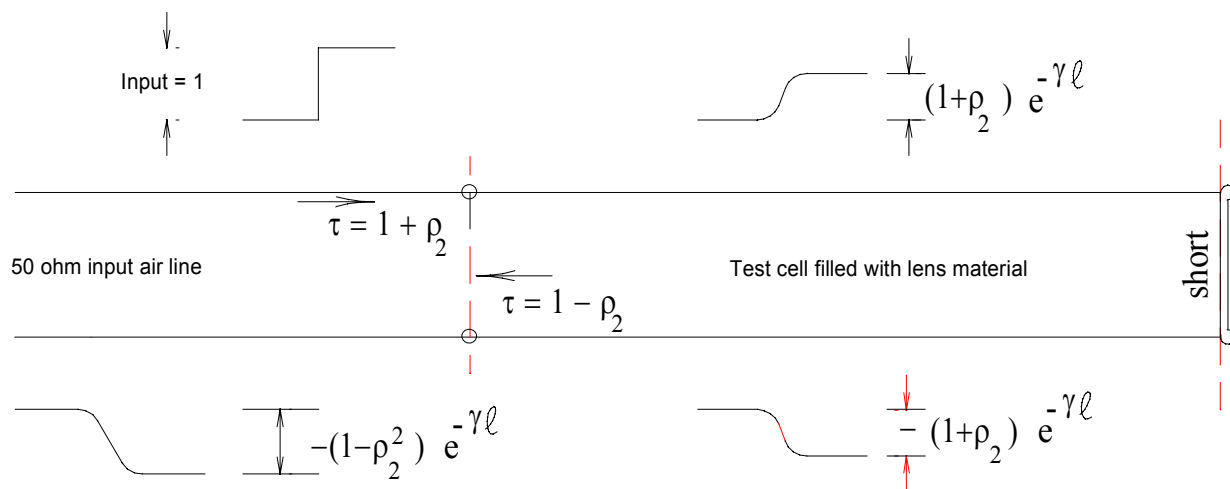


Figure 4-8: Second reflection path.

Here, the input pulse is normalized to unity within the 50 ohm input section. Crossing the interface between the air and the lens material, the input pulse magnitude is multiplied by  $\tau = 1 + \rho_2$ . The pulse continues through the test cell, with complex propagation factor  $e^{-\gamma \ell}$ , until it is reflected out-of-phase by the shorted termination. Retracing its path, the pulse again crosses the lens-material-to-air interface, where it is multiplied by  $\tau = 1 - \rho_2$ .

Two simplifying assumptions are in order. First, the brass short terminating the test cell is a perfect reflector, producing a reflection coefficient of negative one. Second, the reflection coefficient,  $\rho_2$ , is frequency independent. This second assumption is valid for our measurements, because (as shown in the preceding section) the difference between the measured risetimes for the shorted input section and the lens-material-terminated input section is too small to be measured. Given these two assumptions, the frequency response of the lens material becomes:

$$\frac{V_{out}(\omega)}{V_{in}(\omega)} = (1 - \rho_2^2) e^{-(\alpha + j\beta)\ell}, \quad (4-13)$$

where:

$\rho_2$  = constant reflection coefficient at the interface between the air and the lens material,  
 $\ell$  = distance traveled by the pulse ( $2 \times 0.1499$  m for the test cell).

The frequency response is the Fourier transformation of the impulse response. The input step is the negative of (the shorted input section measurement)  $\rho_0$ , and the output step is (the lens-material measurement)  $\rho_3$ . However, since both the input step and the lens-material step are reflected out-of-phase by the terminating short, the effect is as if neither were inverted. Fourier transforming the derivative of the input and output steps and taking their ratio also yields the frequency response:

$$\frac{V_{out}(\omega)}{V_{in}(\omega)} = \frac{fft(\rho'_3)}{fft(\rho'_0)}. \quad (4-14)$$

By equating (4-13) and (4-14), then solving for the propagation coefficient,  $\gamma$ , we obtain:

$$\gamma = \alpha + j\beta = -\frac{1}{\ell} \ln \left( \frac{fft(\rho'_3)}{fft(\rho'_0)} \frac{1}{1 - \rho_2^2} \right), \quad (4-15)$$

where:

$\rho_2$  = constant reflection coefficient at the interface between the air and the lens material,  
 $\rho_3$  = recorded reflection coefficient through the lens material,  
 $\rho_0$  = recorded reflection coefficient of the shorted input section,  
 $\ell$  = distance traveled by the pulse ( $2 \times 0.1499$  m for the test cell).

Equation (4-15) says that measurements: of the reflection of the input step from a perfect short, of the reflection from the air-to-lens-material interface, and of the reflection from a perfect short at the termination of the lens material, are sufficient to determine the propagation coefficient,  $\gamma$ . The complex permittivity is recovered from the propagation coefficient (3-6) as:

$$\varepsilon = \left( \frac{c\gamma}{j\omega} \right)^2. \quad (4-16)$$

#### 4.5.4.2 Data

To make the most accurate measurement possible, we repeated the measurement shown in Figure 4-1 one hundred times. Averaging these repetitions significantly reduced the numerical noise, which can otherwise dominate the differentiated trace. The new data is shown in Figure 4-9, with both traces inverted.

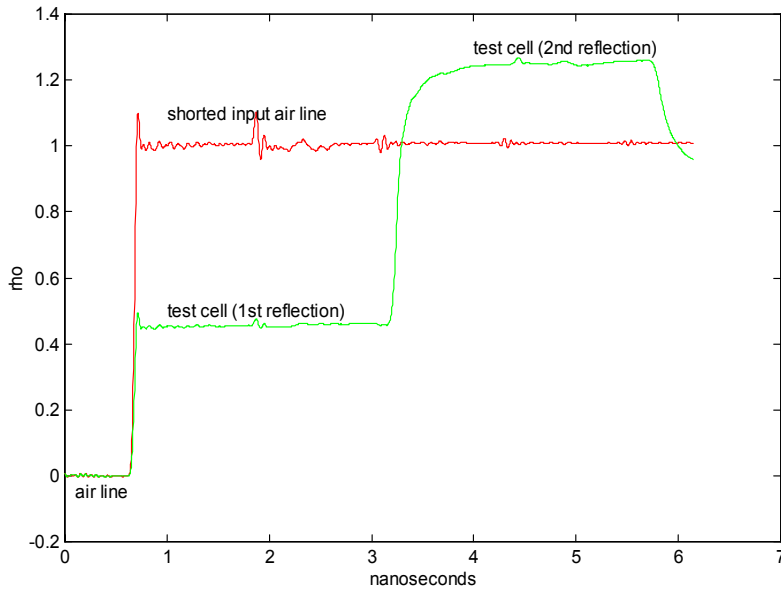


Figure 4-9: Averaged test cell TDR data.

The time-gated derivatives of the data in Figure 4-9 are shown in Figure 4-10. Note that the numerical noise is no longer apparent. The time between the two peaks, the two-way transit time, is still about 2.57 ns, corresponding to a high-frequency value for the dielectric constant of 6.6. This determination agrees well with previously calculated values.

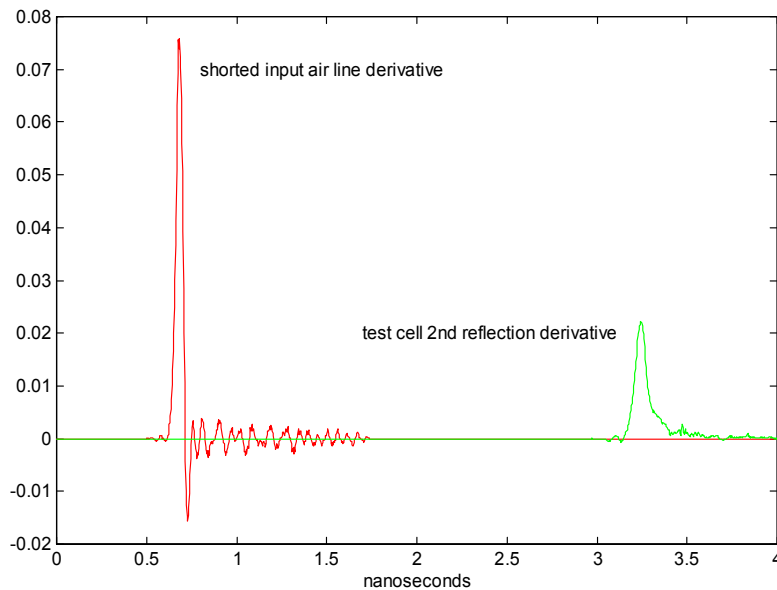


Figure 4-10: Time-gated derivatives of TDR data of input section and test cell.

Figure 4-11 displays the attenuation (real) and phase (imaginary) coefficients,  $\alpha$  and  $\beta$ , of the complex propagation coefficient,  $\gamma$ , as calculated from (4-15). The real propagation coefficient indicates that one meter of lens material would attenuate a pulse by less than one decibel at a frequency of one gigahertz.

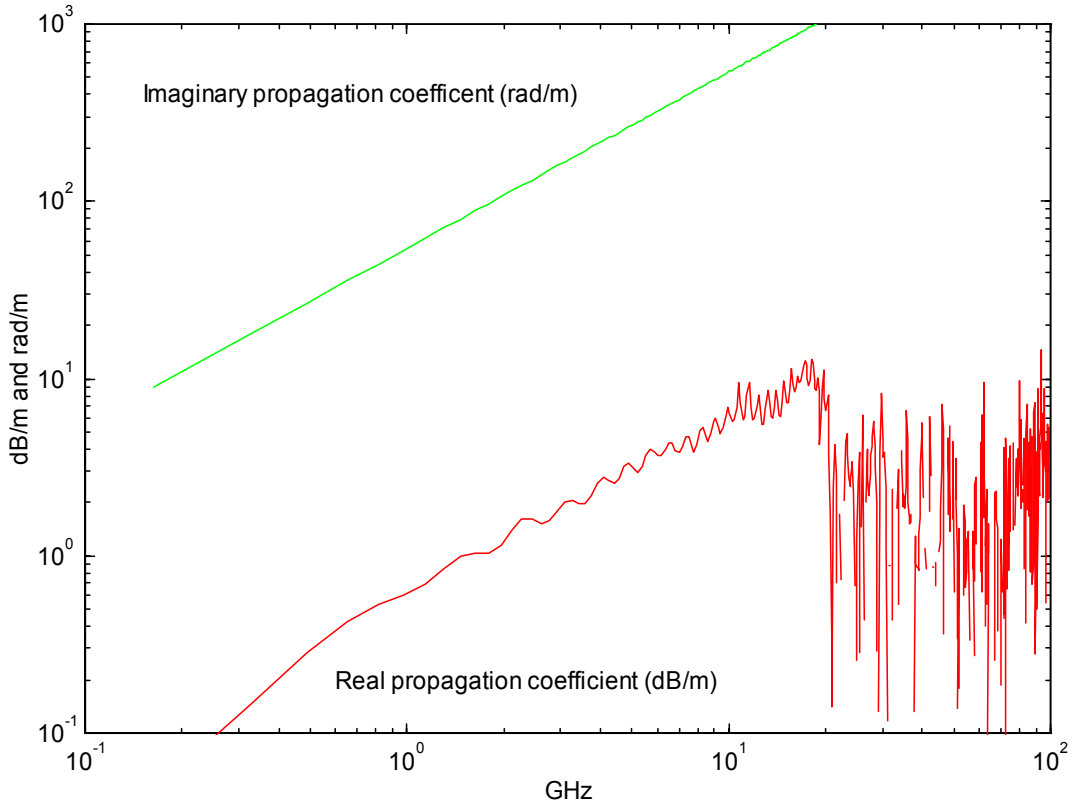


Figure 4-11: Propagation coefficient from second reflection.

Figure 4-12 shows the complex permittivity, as generated from (4-16). The low-frequency dielectric constant is about 7.0; it drops to about 6.5 near 10 GHz. These values for the dielectric constant, as calculated from the propagation coefficient, agree well with the previous measurements, thus validating the propagation coefficient derivation. Above 10 GHz the measurement data are dominated by noise.

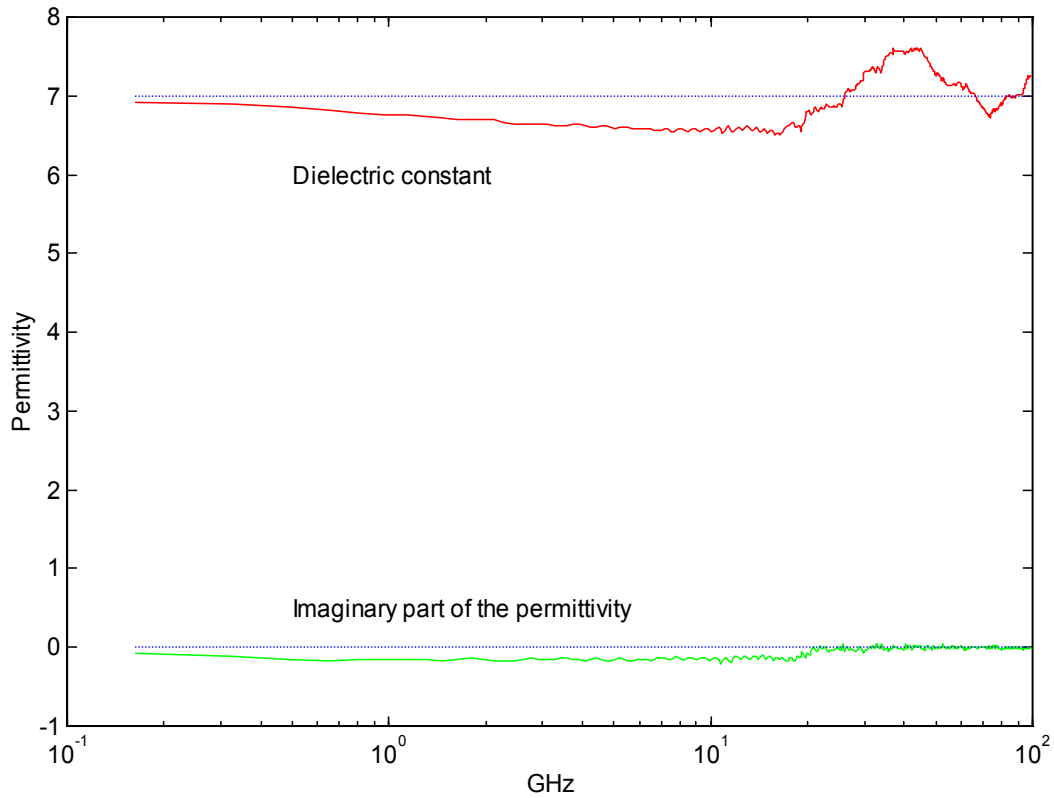


Figure 4-12: Permittivity from second reflection.

#### 4.6 CONCLUSIONS

The measured permittivity of the lens material varies from a low-frequency value of 7.0 to a high-frequency value of 6.5, near 10 GHz. For a pulse with a 100 ps risetime (corresponding to a bandwidth of about 3.5 GHz), the material will have a relative dielectric constant of about 6.6.

At 3.5 GHz, the attenuation coefficient is about 3 dB/m. For the proposed maximum lens thickness of about 8 cm, the attenuation will be about 0.25 dB.

## 5 SCALE-MODEL IMPEDANCE

### 5.1 INTRODUCTION

The scale-model lens mount shows a distinct impedance rise, followed by a drop, at the elliptically shaped transition from the coaxial input section to the lens (refer to Figure 2-4). This impedance variation will cause undesirable reflections and reduce the energy transfer in the full HIRA. We decreased the diameter of the scale-model center conductor in steps, in order to increase the impedance in this area and thus reduce the discontinuity. We tested center conductors with three different minimum diameters: 1.55 mm (0.061 in.), 1.30 mm (0.051 in.), and 0.81 mm (0.032 in.).

### 5.2 PHYSICAL STRUCTURE

Figure 5-1 shows the structure of the scale-model mount, without the lens. In this figure, the center conductor is 1.55 mm (0.061 in.), necking down to 1.30 mm (0.051 in.) where the center conductor leaves the elliptical termination of the coaxial section. In another version of the mount, the diameter of the center conductor did not vary; it was 1.55 mm (0.061 in.). In a third version, the center conductor necked down to 0.81 mm (0.032 in.) for approximately 2.5 mm (0.1 in.), then expanded back up to about 1.27 mm (0.050 in.).

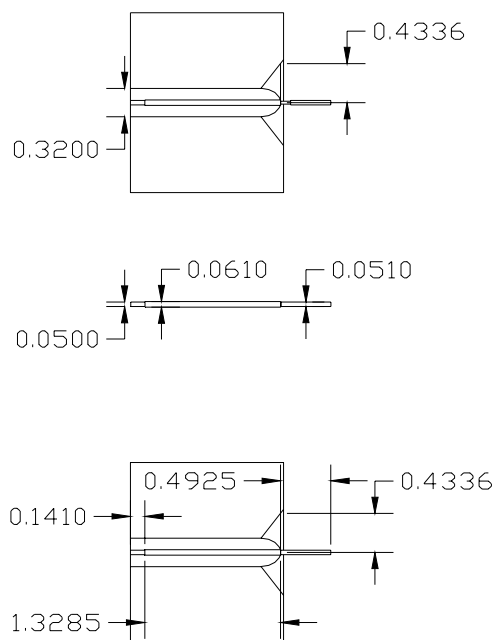


Figure 5-1: Typical scale-model lens mount.

The lens material blank is not shown in the figure. In all three versions, lens material filled the conical space in the aluminum mount and extended, as a one-inch cylindrical lens blank, to just beyond the end of the center conductor. The region of interest here is the volume filled by the lens material, i.e., the region from the elliptical end of the Teflon insert, to just past the aluminum mounting block.

### 5.3 THEORETICAL IMPEDANCE

The impedance is given by the following equation, based on the coaxial geometry and assuming a dielectric constant corresponding to a homogeneous mixture of Teflon and lens material:

$$Z = 60 \ln \left( \frac{d_{lensMat}}{d_{cc}} \right) \sqrt{\frac{\epsilon_{LensMat} \ln \left( \frac{d_{LensMat}}{d_{Teflon}} \right) + \epsilon_{Teflon} \ln \left( \frac{d_{Teflon}}{d_{cc}} \right)}{\epsilon_{LensMat} \epsilon_{Teflon} \ln \left( \frac{d_{LensMat}}{d_{cc}} \right)}}, \quad (5-1)$$

where:

- $d_{LensMat}$  = outer diameter of the lens material,
- $d_{cc}$  = outer diameter of the center conductor,
- $d_{Teflon}$  = outer diameter of the Teflon,
- $\epsilon_{LensMat}$  = dielectric constant of lens material,
- $\epsilon_{Teflon}$  = dielectric constant of Teflon.

Figure 5-2 shows the theoretical impedance of the three scale-model lens mounts.

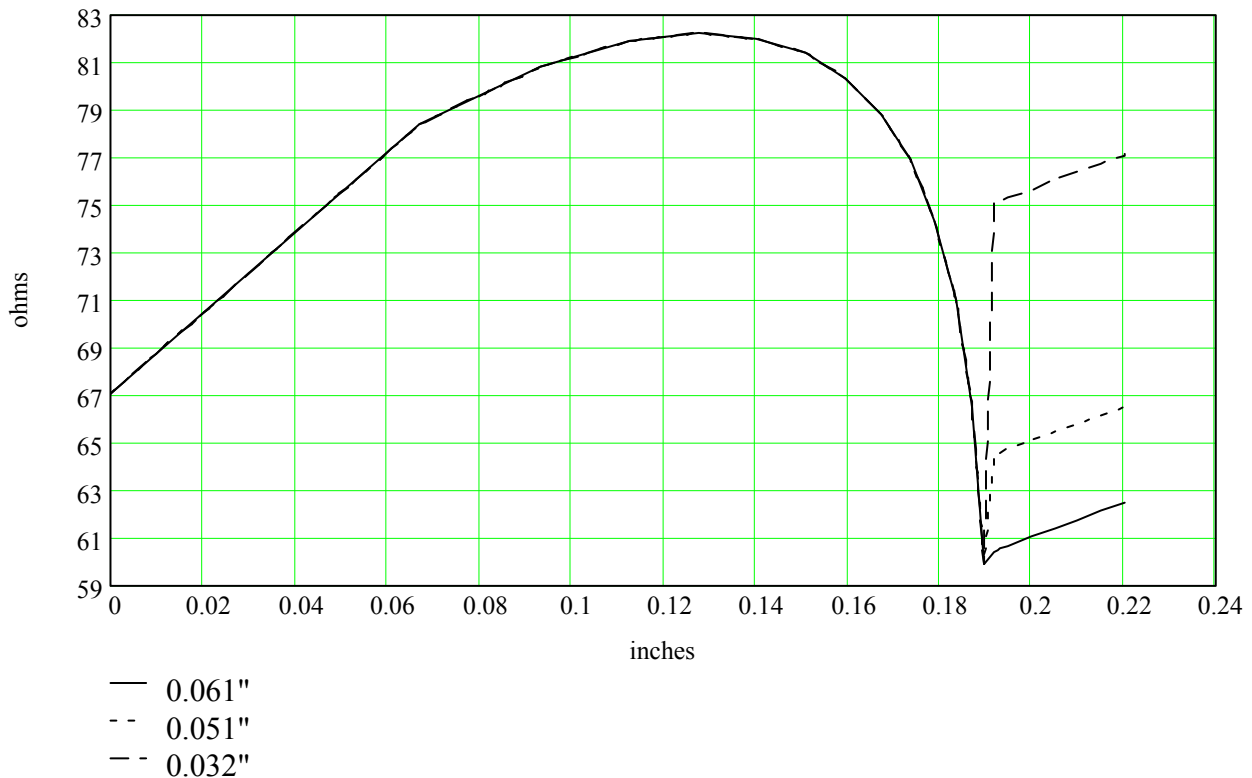


Figure 5-2: Theoretical impedance of three scale-model lens mounts. Simple coaxial geometry is assumed. Minimum center conductor diameters are indicated.

In this figure, zero is the start of the elliptical terminating section of the Teflon material. Up to that point, the impedance is a constant 67 ohms. For all three mounts, the impedance increases for the next 3.3 mm (0.13 in.) to about 82 ohms, then decreases rapidly to 60 ohms at

about 4.8 mm (0.19 in.) where the center conductor exits the Teflon. At this point, the end of the Teflon, the diameter of the center conductor varied from 0.81 mm (0.032 in.) to 1.55 mm (0.061 in.) for the three mounts. The result of the impedance calculation is a narrow notch (always to 60 ohms), the height of which is determined by the impedance of the continuing aluminum conic section, the dielectric constant of the lens material, and the diameter of the center conductor.

#### 5.4 MEASURED IMPEDANCE

We measured the impedance of all three lens mounts using the 11801B sampling oscilloscope configured with the SD 24 TDR sampling head. Figure 5-3 shows the results. The data in the figure have been windowed and filtered, and the input step has been deconvolved. Some of the ringing visible here results from the abrupt termination of the data.

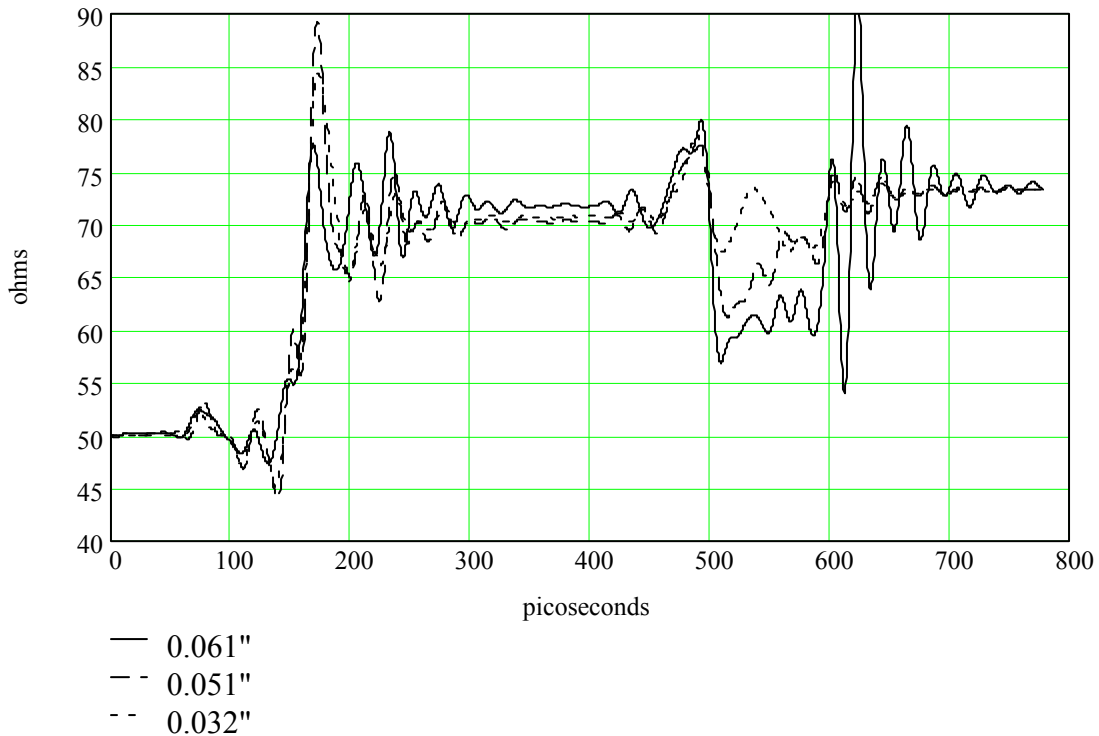


Figure 5-3: Measured impedance of three scale-model lens mounts. Minimum center conductor diameters are indicated.

Note that the step output of the SD 24 TDR sampling head for the 11801B oscilloscope has a 30 ps risetime. The physical length of the ellipsoid section of the Teflon is about 4.8 mm (0.19 in.), corresponding to a transit time of about 24 ps. Over that time, the impedance rises to about 80 ohms, falls to about 60 ohms, then starts rising again. This impedance variation occurs too quickly to be characterized by the 30 ps risetime of the TDR.

This impedance variation appears in the figure from about 450 ps to about 510 ps. The time lengthening is due to the later return of reflections traveling through the higher-dielectric-

constant lens material, in addition to the effect of the TDR step risetime. The transit time through the lens material is about 43 ps.

The impedance notch, visible in Figure 5-2 for the 1.30 mm (0.051 in.) and 0.81 mm (0.032 in.) center conductor mounts, cannot be seen in the measured data. The width of this notch is at most 0.5 mm (0.02 in.), corresponding to about 4.5 ps in the lens material. This time-duration is too short to be resolved by the TDR.

## 5.5 RADIATING ARM IMPEDANCE

The HIRA radiating elements are designed to have a combined impedance of 100 ohms. Each element, with the reflection of the other element, forms a structure with an impedance of 200 ohms, so the impedance of the parallel combination of the two elements and their reflections is 100 ohms. In Section 2.2 the half-angle of each cone was found to be 4.09 degrees. The 4.09 degree half-angle cannot extend to the parabolic reflector rim because the cone would intersect the reflector well before the rim. For this reason, the elements must start narrowing so as to approach a point at the rim (refer to Figures 2-1 and 2-3).

The narrowing of the radiating arms increases the biconic impedance; but, because the impedance of the HIRA structure starts decreasing, the two effects tend to cancel. The structural impedance of the HIRA starts decreasing, because the field reflected by the parabolic dish is intercepted by the radiating elements, thus modifying the voltage and current in the elements, as discussed below.

The radiating elements produce a spherical wave radiating from the biconic origin. The origin is at the parabolic focal point, 7.6 cm (3 in.) from the parabolic vertex. The wave propagates outward from the origin. At the parabolic dish, the electric field reflects out-of-phase and the magnetic field reflects in-phase. The reflected field is intercepted by radiating elements, where the inverted electric field generates a voltage that tends to cancel the original driving voltage, and the in-phase magnetic field generates a current tending to reinforce the original driving current. Thus, the impedance starts to decrease at a time corresponding to that required to complete a round trip over the 7.6 cm distance from the origin to the vertex. To oppose this impedance decrease, the taper of the radiating elements is reversed at a point 7.6 cm from the origin, thus increasing the biconic impedance.

This impedance behavior can be seen in the TDR of the complete HIRA scale-model in Figure 5-4. In this figure, the HIRA lens-material starts about 0.7 ns. Shortly before 0.8 ns, the lens ends and the radiating elements start. The TDR shows the biconic impedance to be about 100 ohms, as expected, until 0.5 ns later (1.3 ns in the figure), when the impedance starts dropping. The dropping impedance is caused by the reflected wave reducing the voltage-to-current ratio in the radiating elements. Finally the cones terminate in the 100 ohm resistive termination, apparent at 1.8 ns, where the impedance starts increasing.

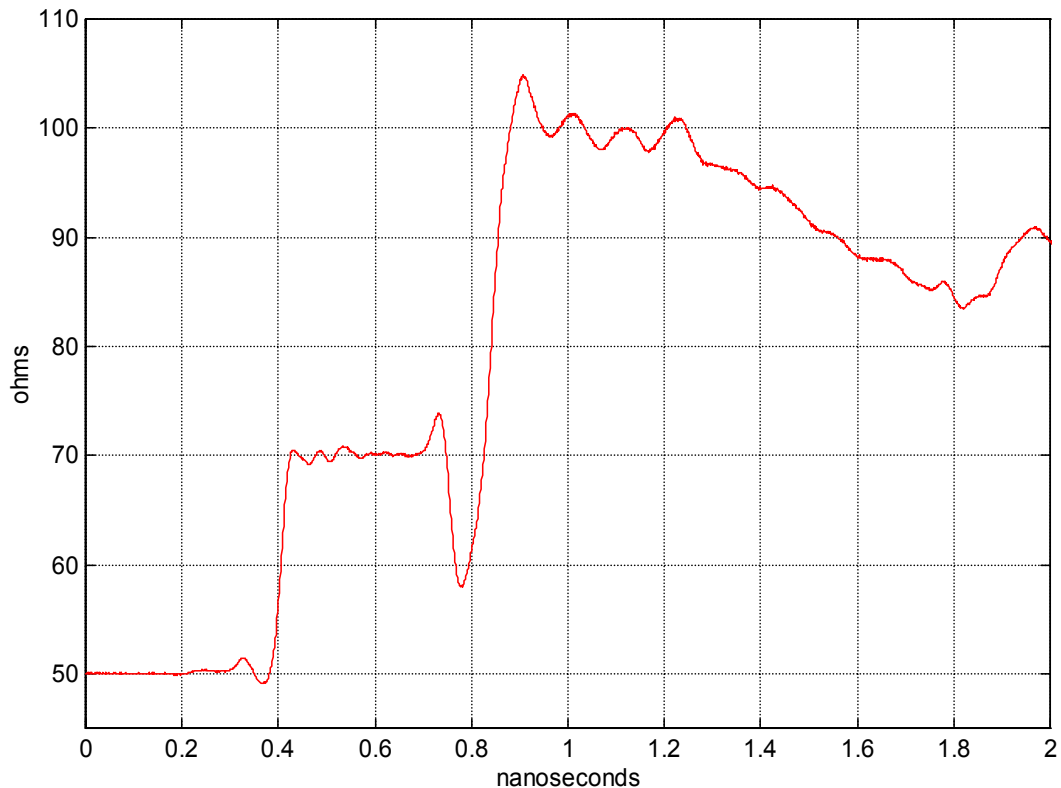


Figure 5-4: Impedance of the scale-model HIRA, including radiating elements.

## 5.6 CONCLUSIONS

The impedance rise to 80 ohms in the lens is real, unavoidable, and will occur in the full-scale HIRA.

The impedance drop to 60 ohms is real. Reducing the center conductor diameter immediately following the elliptical oil dielectric section will make the impedance discontinuity so short in time that it will have negligible effect on the longer-risetime pulse of the final full-scale configuration. The discontinuity will probably be large enough to measure using the 11801B SD 24 TDR sampling head.

The impedance of the radiating elements will not be a constant 200 ohms. The impedance will start diminishing after the round-trip time from the origin of the elements to the parabolic dish. This implies that the distance from the origin corresponding to this time is a reasonable place to start reversing the cone taper. Reversing the taper at this point will tend to make the cone impedance more constant.

## 6 ELECTRIC FIELD MEASUREMENTS

The original scale-model HIRA (without the lens) and the new scale-model HIRA (with the lens) were mounted on a ground-plane and driven with a voltage step. The resultant electric fields were recorded. The measured electric fields compare well, indicating that the lens and associated coaxial mount structure have no detrimental effect on the radiated fields. Both measured fields compare well to the predicted field.

### 6.1 EQUIPMENT SETUP

Figure 6-1 shows the scale-model HIRA mounted on the 2.44 m (8 ft) long and 1.83 m (6 ft) wide aluminum ground-plane used to make the electric-field measurements. The electric field is sensed by an EG&G, ACD-9, D-dot sensor. Both the HIRA and the ACD-9 are mounted on the centerline of the ground-plane.

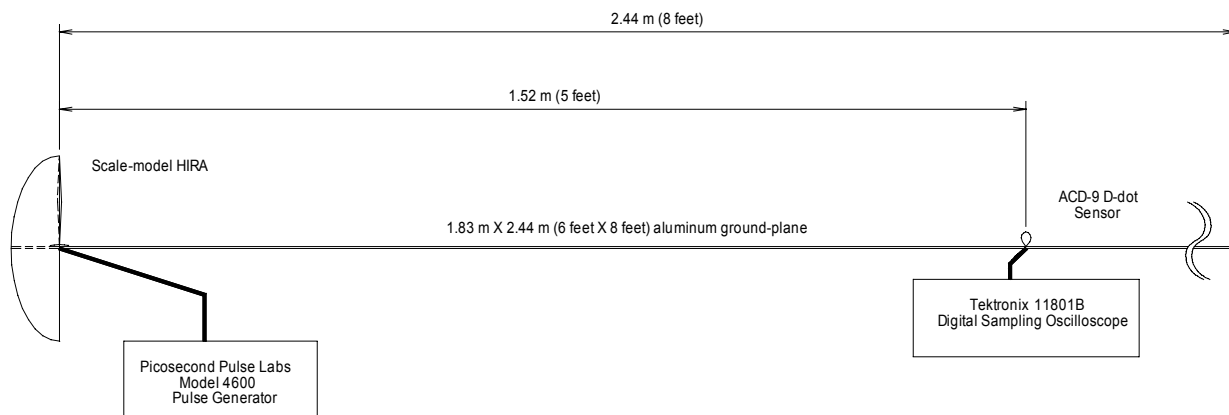


Figure 6-1: Scale-model E-field measurement instrumentation.

A Picosecond Pulse Labs (PPL) model 4600 generator drives the HIRA with a 21 volt step pulse into a 50 ohm load. The pulse risetime is 75 ps. Since the PPL step generator has a 50 ohm output and the HIRA radiating elements have a paralleled impedance of 100 ohms, the step voltage seen at the input to the radiating elements is 28 volts (see (4-2)).

A Tektronix 11801B Digital Sampling Oscilloscope records the ACD-9 response. Step generator and oscilloscope are connected to the HIRA and sensor with 30 cm (12 in.) sections of semi-rigid coaxial cable fitted with SMA connectors.

### 6.2 PREDICTED FIELD DATA

We use the predicted field for a two-element IRA to derive an expression for the HIRA. A two-element IRA is shown schematically in Figure 6-2A. The theoretical electric field generated by a two-element IRA driven by a step voltage,  $V$ , is given in [5] as:

$$E(r, t) = \frac{D}{4\pi c f_g r} \left[ \frac{dV(t - 2F/c)}{dt} - \frac{c}{2F} \left( V(t) - V\left(t - 2\frac{F}{c}\right) \right) \right], \quad (6-1)$$

where:

- $E$  = electric field, in V/m,
- $D$  = diameter of the reflector, in meters,
- $V$  = step voltage between the drive arms,
- $f_g$  = ratio of HIRA input impedance to free space (400/377),
- $r$  = distance from the HIRA, in meters,
- $F$  = focus of the parabolic reflector, in meters,
- $c$  = velocity of propagation, meter/second.

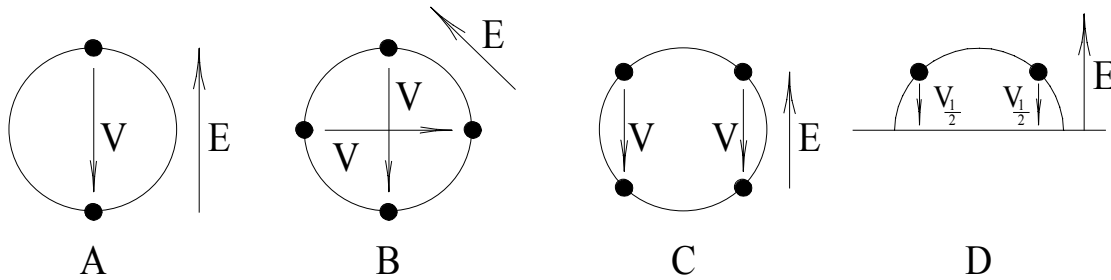


Figure 6-2: Schematic formation of a HIRA from a two-element IRA

Figure 6-2B shows the IRA with two additional arms. Adding these two arms generates a rotated resultant field increased by the square root of two. Rotating the entire IRA by 45 degrees results in Figure 6-2C. Adding an infinite ground-plane through the horizontal symmetry plane and reducing the driving voltage by a factor of two results in Figure 6-2D. Although the driving voltage is reduced, the electric field remains unchanged, due to the contribution from the reflection in the infinite ground plane. Figure 6-2D is a good approximation of the physical HIRA, where the ground-plane appears essentially infinite.

Doubling (6-1) and multiplying by the square root of two accommodates the changes from the two-armed IRA to the HIRA (i.e. accounts for the reduced drive voltage and the superposition of the fields from the two additional elements). The result is:

$$E(r, t) = \frac{2\sqrt{2}D}{4\pi c f_g r} \left[ \frac{dV_{1/2}(t - 2F/c)}{dt} - \frac{c}{2F} \left( V_{1/2}(t) - V_{1/2}(t - 2\frac{F}{c}) \right) \right], \quad (6-2)$$

where:

$V_{1/2}$  = step voltage on the drive arm with respect to the ground plane.

Use of (6-2) with an analytic pulse having a 75 ps risetime and a 28 volt step, yields the theoretical electric field shown in Figure 6-3. This is the field predicted for the scale-model HIRA at 1.52 m (5 ft) on the centerline.

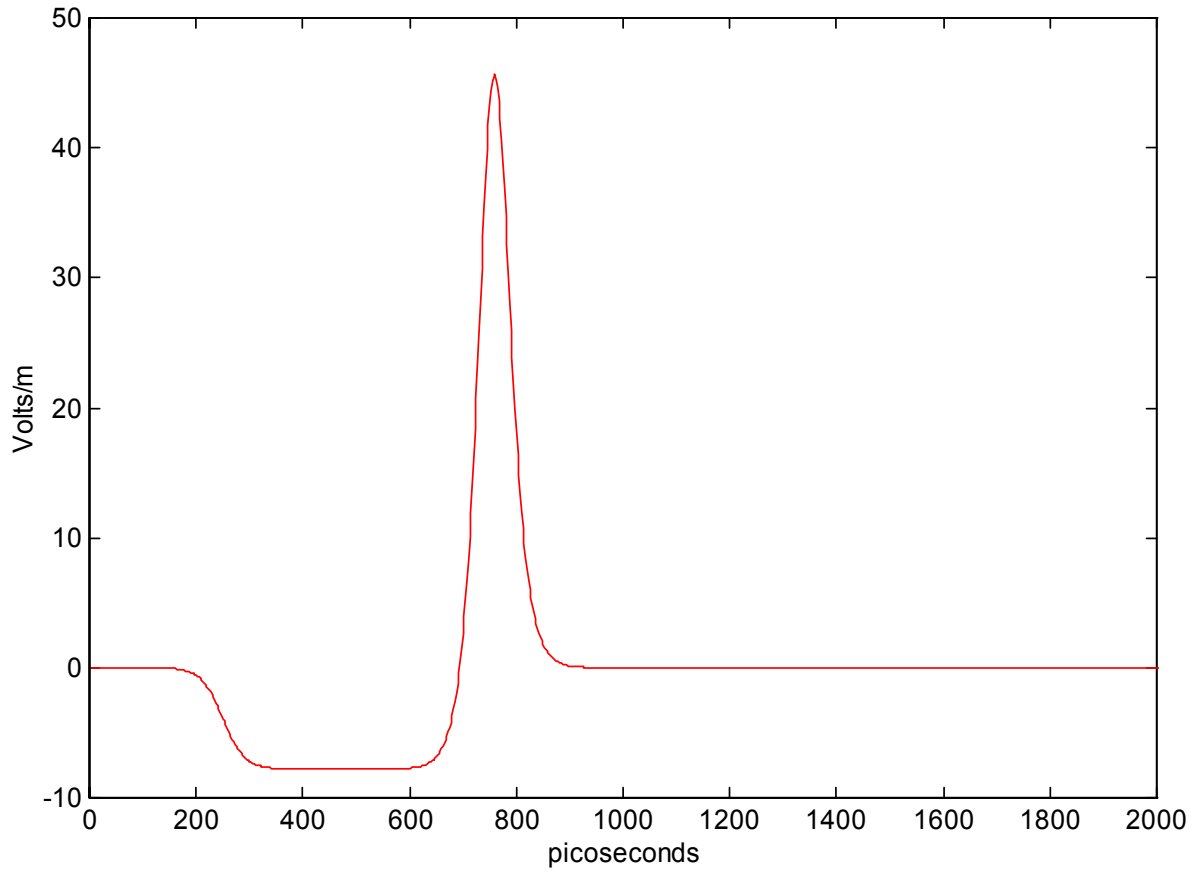


Figure 6-3: Theoretical electric field on the centerline at 152 cm from the scale-model HIRA.

### 6.3 COMPARISON THEORETICAL AND MEASURED ELECTRIC FIELDS

Figure 6-4A shows a comparison of the theoretical electric field, as calculated from (6-2), with the measured electric fields. Figure 6-4B shows the same data with an expanded time base. The measured fields for both the original HIRA, with no lens, and the new HIRA, with lens, are shown. The measured data in this figure have been converted to units of volts/meter by integrating the measured sensor voltage and deconvolving the ACD-9 sensor response.

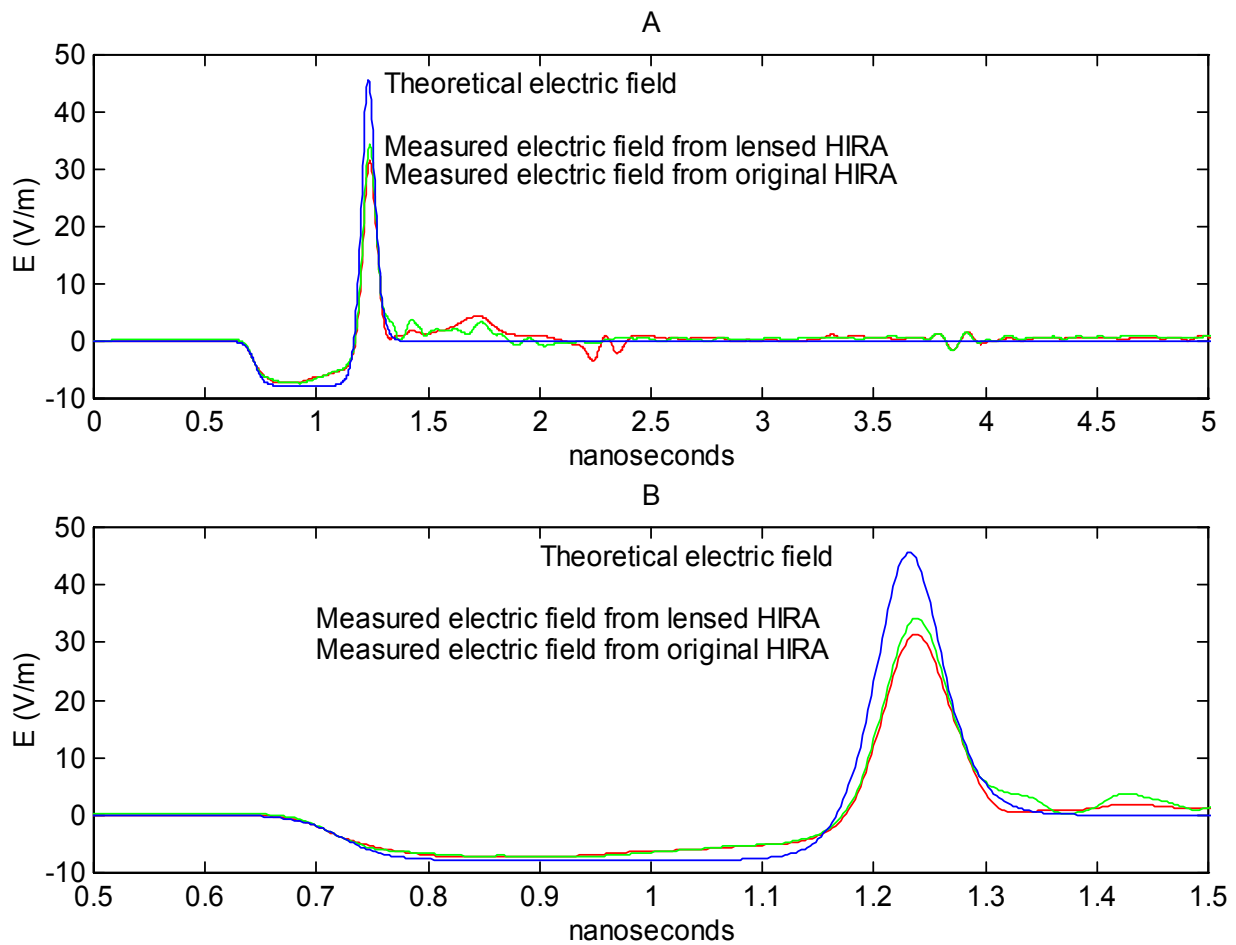


Figure 6-4: Comparison of the measured and theoretical electric fields.

Figure 6-4 shows that both HIRAs have similar responses. The lensed HIRA shows a slightly larger response than original HIRA. Both have peaks at approximately seventy percent of the theoretical peak value.

#### 6.4 HIRA STEP RESPONSE AND IMPULSE RESPONSE

Deconvolution of the input voltage step and cable response from the measured electric field and its derivative generates the HIRA step and impulse responses. Figure 6-5A shows the impulse response for both the lensed and unlensed HIRAs. Figure 6-5B shows the step responses for the HIRAs.

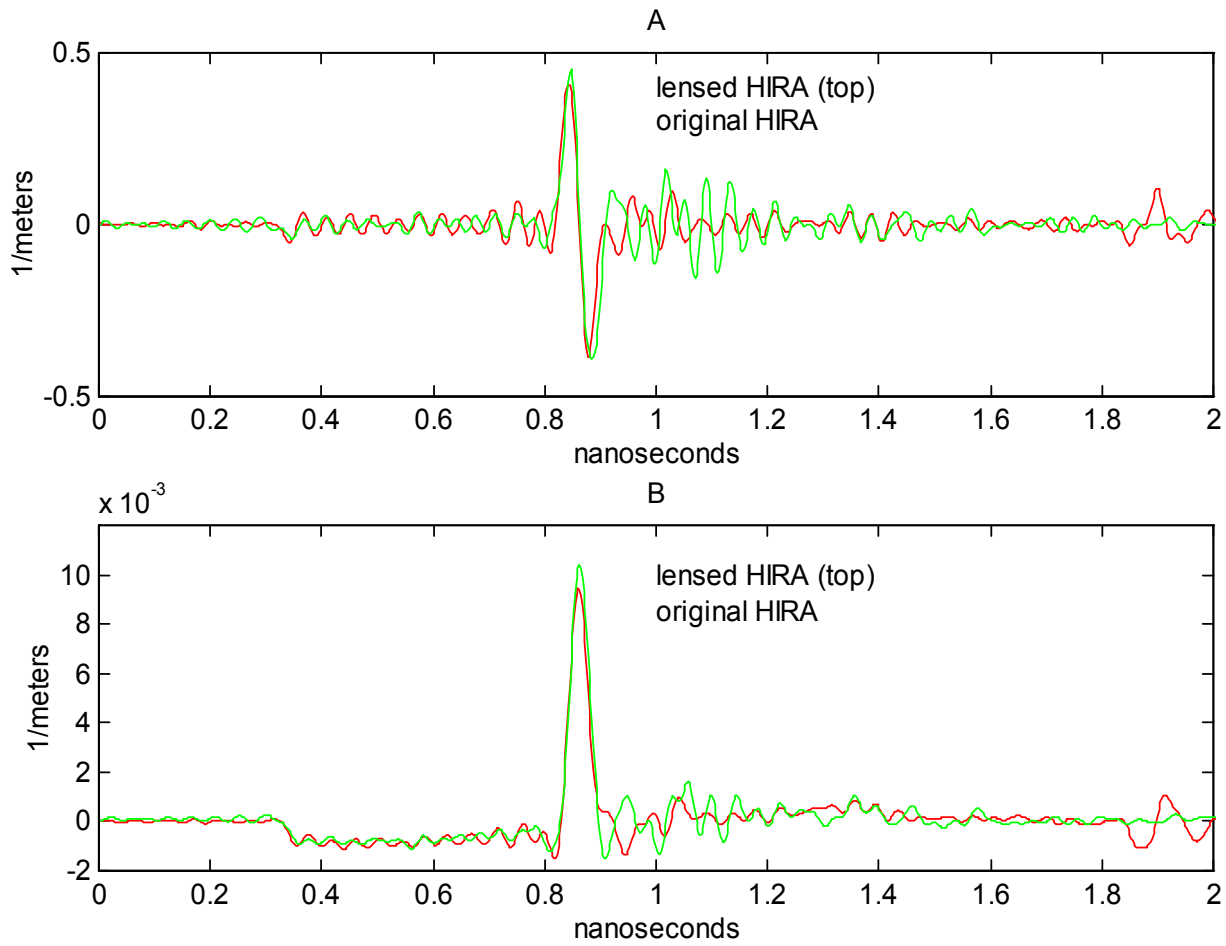


Figure 6-5: HIRA impulse (A) and step (B) responses.

#### 6.5 CONCLUSIONS

The lens has little effect on the radiated field. Both HIRAs exhibit good agreement with the predicted electric field.

## 7 HIGH VOLTAGE TESTING

To ensure that the lens material would be capable of withstanding the expected electric field strength generated within the lens, we tested several disks of the material. Figure 7-1 shows the test setup. A disk is suspended between the two aluminum balls. Then voltage is applied to the attached brass rods from two high-voltage, dc generators in series. We tested six-centimeter-diameter disks of various thickness. Each disk was milled to a uniform thickness over the tested central portion.

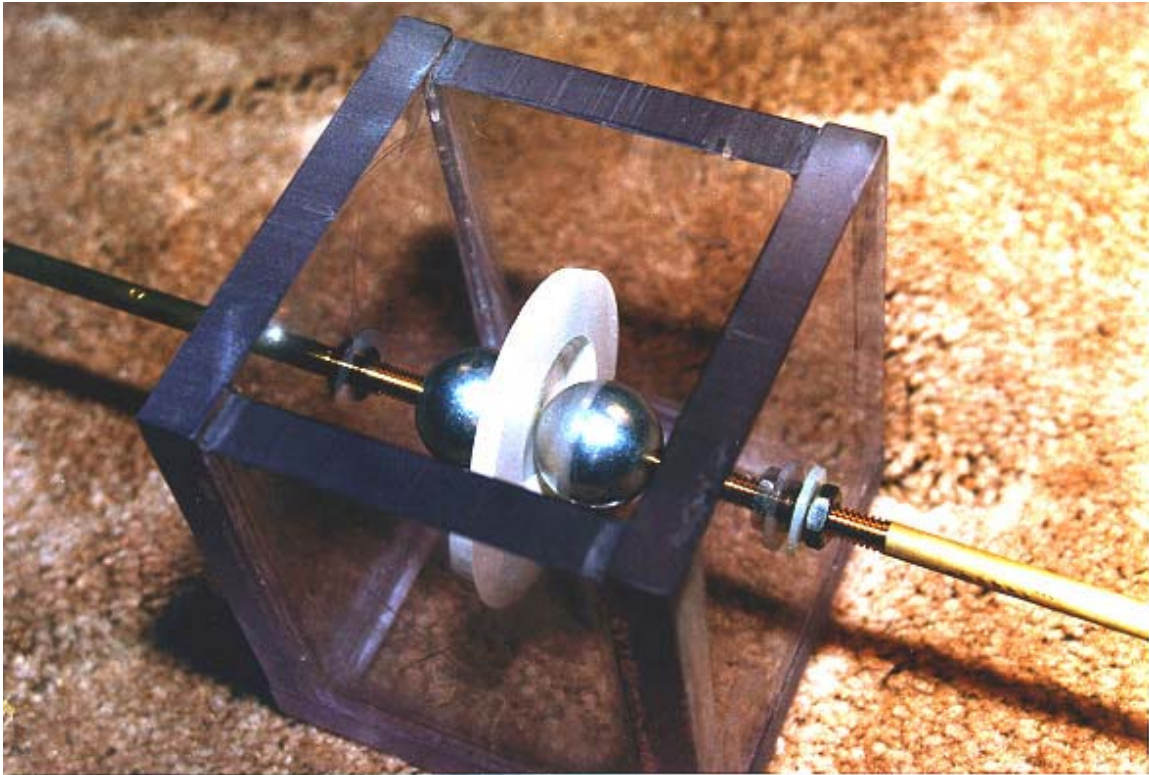


Figure 7-1: High voltage test fixture.

### 7.1 TESTING

Each disk was held in place between the aluminum electrodes by pressure generated from the threaded brass rods. During the first series of tests, without transformer oil in the tank, the high voltage tracked around the disk, rather than punching through. The thinnest disk tested was 1.37 mm thick. Arcing around this disk occurred at about 32 kV. After we added transformer oil to completely submerge this test disk, it withstood 70 kV without failing. At 70 kV, corona formation and transformer oil rolling were sufficiently pronounced to terminate the experiment.

Even with vacuum evacuation of the disks during curing, some voids form. We were unable to mill a full sized disk to a significantly smaller thickness, because of these voids, and because the thin disk was too fragile. To circumvent this problem, we used a thicker disk and milled down only a small (approximately 2.5 mm diameter) center section. This center section was 0.762 mm (30 mil) thick, with no visible voids.

When immersed in transformer oil, this disk failed at 50 kV, corresponding to 65.6 MV/m (1.7 kV/mil). The failure mode was a clearly visible hole punched through the milled-down section of the disk.

## 7.2 WORST-CASE DC VOLTAGE REQUIREMENT

Figure 7-2A shows a simplified drawing of the lens structure for the full-scale HIRA. In this figure, the center conductor necks down to 0.81 cm at its narrowest point. The following calculations assume a 1 MV pulse driving the HIRA.

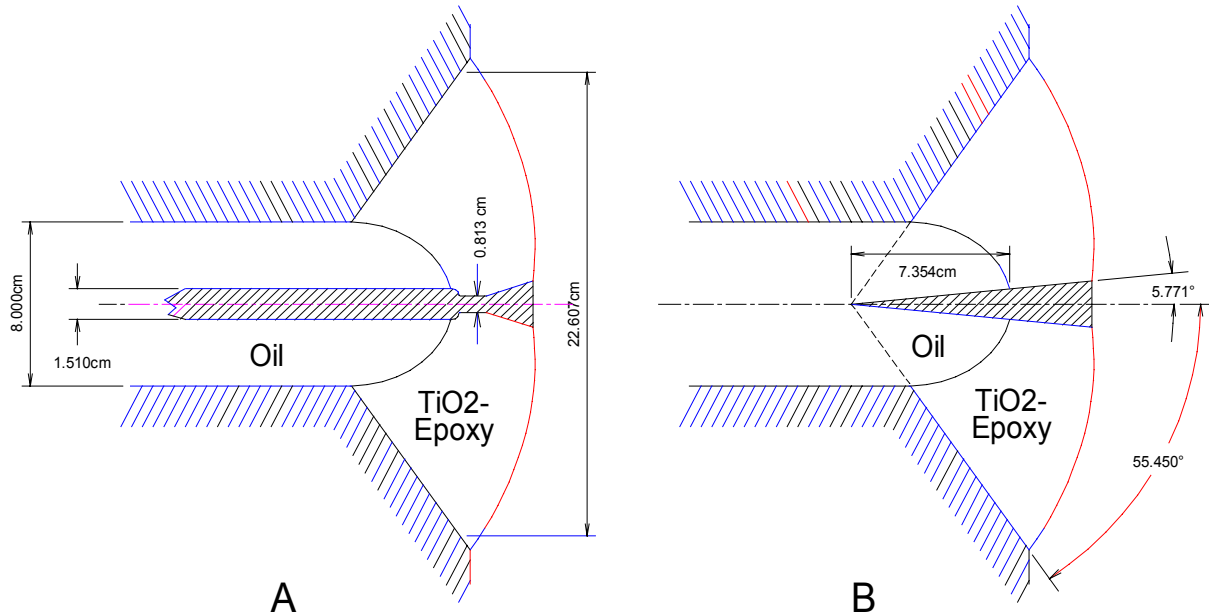


Figure 7-2: Simplified drawings of the lens structure for the full-scale HIRA.

### 7.2.1 Lens Structure Considered as a Coaxial Transmission Line.

The maximum electric field in a coaxial transmission line is generated at the center conductor as:

$$E_{\max} = \frac{V}{d \ln\left(\frac{D}{d}\right)}, \quad (7-1)$$

where:

- $E_{\max}$  = maximum electric field within the coaxial structure,
- $V$  = voltage between the inner conductor and outer conductor,
- $d$  = diameter of the inner conductor,
- $D$  = diameter of the outer conductor.

Within the oil-filled coaxial structure, the highest field will occur at the center conductor. In the oil, the diameter of the center conductor is 1.51 cm, and the diameter of the outer conductor is approximately 8 cm. From (7-1), the maximum electric field will be 40 MV/m.

A reflection occurs where the center conductor attaches to the radiating elements, if the impedances do not match. The impedance of the radiating elements is 100 ohms. The impedance of a simple coaxial structure is given by:

$$Z_{coax} = \frac{60}{\sqrt{\epsilon_r}} \ln\left(\frac{D}{d}\right), \quad (7-2)$$

where:

$Z_{coax}$  = impedance within the coaxial structure,  
 $\epsilon_r$  = relative permittivity (dielectric constant = 2.2 for oil).

For the HIRA coaxial section, (7-2) produces an impedance of 67 ohms. Following the reasonably smooth transitional lens, the impedance of the 100 ohm radiating elements appears at the attachment point. A 67 ohm to 100 ohm impedance jump has a reflection coefficient of about 0.20; so the maximum electric field generated is twenty percent higher than the 40 MV/m predicted by (7-1). The simple coaxial model thus predicts a maximum field of about 48 MV/m.

## 7.2.2 Lens Structure Considered as a Biconic TransmissionLine.

Figure 7-2B shows the HIRA lens area modeled as a biconic transmission line. From [6], the impedance and electric field for a biconic transmission line are given as (7-3) and (7-4), respectively:

$$K = \frac{\eta}{2\pi} \ln\left(\tan\frac{\theta_2}{2} \cot\frac{\theta_1}{2}\right), \quad (7-3)$$

where:

$K$  = biconic impedance,  
 $\eta$  = intrinsic impedance of the dielectric material ,  
 $\theta_1$  = half-angle of center conductor cone (5.8 degrees in Figure 7-2B),  
 $\theta_2$  = half-angle of the outer conductor cone (55.5 degrees in Figure 7-2B).

and

$$E_\theta = \frac{\eta V}{2\pi r K \sin(\theta_1)}, \quad (7-4)$$

where:

$r$  = radial distance along the centerline from the apex.

Combining (7-3) and (7-4) generates (7-5) for the electric field in terms of the voltage, conic half-angles, and distance from the conic apex:

$$E_\theta = \frac{V}{r \ln\left[\tan\left(\frac{\theta_2}{2}\right) \cot\left(\frac{\theta_1}{2}\right)\right] \sin(\theta_1)}. \quad (7-5)$$

With  $r = 7.354$ , and the simplifying assumption of a homogenous dielectric, the half-angles given in Figure 7-2B produce an approximate electric field at the oil-lens-material interface of 58 MV/m.

At the interface, the dielectric constant changes from 2.2 for the oil to 7.0 for the lens material. Since the dielectric constant for the lens material is greater than that of the oil, the intrinsic impedance of the lens material is less than that of the oil. The lower impedance results in a negative reflection coefficient determined as:

$$\rho = \frac{\sqrt{\epsilon_1} - \sqrt{\epsilon_2}}{\sqrt{\epsilon_1} + \sqrt{\epsilon_2}}, \quad (7-6)$$

where:

- $\rho$  = reflection coefficient of the boundary between the oil and lens material,
- $\epsilon_1$  = dielectric constant of the oil (2.2),
- $\epsilon_2$  = dielectric constant of the lens material.

Near the coaxial section, the lens structure approximates a bicone in oil. From (7-3), the impedance of the oil-filled bicone is 95 ohms. Near the radiating elements, the lens structure appears as a bicone filled with lens material. The impedance of this structure is 53 ohms. These values agree, qualitatively, with the impedance calculations and measurements of Section 5. Upon entering the lens domain, but while still within the oil, the structural impedance rises above 67 ohms. In the section consisting only of lens material, the impedance falls below 67 ohms.

Eventually the pulse encounters the 100 ohm impedance of the radiating elements. As a worst case, assuming the lens to have a negligible effect due to the short transit time, the electric field will be increased by the reflection caused by the transition from the 67 ohm coaxial region to the 100 ohm radiating-element region, as in Section 7.2.1. For the 58 MV/m field calculated from the biconic electric field, the rise from 67 ohms to 100 ohms will increase the field strength to 70 MV/m.

### 7.3 CONCLUSIONS

The measured threshold breakdown field strength for the lens material is 65 MV/m for dc conditions. The coaxial and biconic models predict electric fields in the lens structure of 48 MV/m and 70 MV/m, respectively. However, these fields exist only at the peak of very short-duration voltage pulses. The measured breakdown strength is for dc fields, and cannot be directly related to very short-pulse breakdown. One would expect a good dielectric to withstand pulsed voltages at least an order of magnitude higher than for dc voltage. Since the predicted pulsed field magnitudes are on the same order as the measured dc breakdown threshold, there is an adequate safety margin.

## References

1. Sower, G. D., L. M. Atchley, D. E. Ellibee and E. G. Farr, *Scale-Model Ground-Plane Measurements of a Half IRA*, Prototype IRA Memo 6, January 1996.
2. Bigelow, W. S., E. G. Farr, and G. D. Sower, *Design Optimization of Feed-Point Lenses for Half Reflector IRAs*, Sensor and Simulation Note 400, August 1996.
3. Daniel, V. V., *Dielectric Relaxation*, Academic Press, NY, 1967.
4. Guillemin, E. A., *Synthesis of Passive Networks*, J. Wiley & Sons, NY, 1957.
5. Farr, E. G., and C. A. Frost, *Compact Ultra-Short Pulse Fuzing Antenna Design and Measurements*, Sensor and Simulation Note 380, June 1995.
6. Schelkunoff, S. A., and H. T. Friis, *Antennas, Theory and Practice*, John Wiley & Sons, Inc., NY, 1952, p 105-106.